



Plasmonic Photocatalysis of Urea Oxidation and

Visible Light Fuel Cells

Xingda An^{1, 2}, David Stelter¹, Tom Keyes¹ and Björn M. Reinhard^{1, 2, 3*}

¹Department of Chemistry, Boston University, Boston, MA 02215, United States.

²Photonics Center, Boston University, Boston, MA 02215, United States.

³Lead Contact

*Correspondence: bmr@bu.edu.

SUMMARY

The intense electric (E-) field associated with the localized surface plasmon resonance (LSPR) of noble metal nanoantennas provides a rational strategy to enhance photoinduced charge transfer in photocatalysts. Here, we demonstrate E-field-enhanced direct photocatalytic urea oxidation and a visible light-driven Direct Urea Fuel Cell (LDUFC) with tris(bipyridine)Ruthenium(II), [Ru(bpy)3]²⁺,-enabled plasmonic nanopigments that contain a phospholipid membrane self-assembled around a Ag nanoparticle (NP) whose LSPR overlaps with the [Ru(bpy)3]²⁺ metal-to-ligand charge transfer (MLCT). In the hierarchical plasmonic nanopigment design, the membrane serves as scaffold and spacer to localize [Ru(bpy)3]²⁺ in an electromagnetic "sweet spot" where substantial plasmonic enhancement of photoexcitation is achieved while strong metal-associated quenching of the reactive excited state is avoided. The demonstration of plasmon-enhanced photocatalytic urea oxidation and the implementation of LDUFC represent important advancements towards improved light-driven waste water treatment and efficient solar energy conversion.

Plasmonic Catalysis, Nanoantenna, Electric Field, tris(bipyridine)Ruthenium(II), Metal to Ligand Charge Transfer, Localized Surface Plasmon Resonance, Photoconversion, Photocatalysis, Urea, Fuel Cell.





INTRODUCTION

Solar energy conversion through photocatalysis of chemical bond formation and photo fuel cells are examples of photoharvesting processes that benefit from optimized photocatalysts. Intriguingly, the excitation of LSPRs in noble metal nanoparticles (NPs) provides unique opportunities for enhancing photochemistry through different forms of plasmonic catalysis. While plasmon decay-induced hot charge carrier formation has been demonstrated to contribute to noble metal direct heterocatalysis¹⁻³ and catalysis facilitated by metal-semiconductor junctions;⁴⁻⁸ the resonant electric (E-) fields generated from LSPRs offer a powerful alternative approach for amplifying molecular transitions-mediated photocatalysis. 9-15 A major challenge for E-field-driven plasmonic catalysis concepts is, however, the need to balance E-field-enhanced absorption rates with the quenching of the photoexcited state through the metal. In practice, for NPs with diameters of around 45 nm, as used in this work, separations between the NP surface and photocatalysts < 5 nm are required to substantially boost absorption through the strong local E-field, 4, 16-19 but for even smaller separations (< 2 nm), strong quenching of excited states through the metal surface becomes dominant.²⁰⁻²² The viability of plasmonic E-field enhancement of photocatalysis has been demonstrated primarily with semiconductor photocatalysts. 11-15 For less robust but potentially more versatile and selective photoreactive molecular catalysts, the effect of the E-field enhancement is less well understood, 9-10 and the realization of enhanced hybrid systems is challenged by the need for reliable positioning of the photocatalysts at desirable separations from the metal NP surface. In this manuscript, we explore the quantitative optimization of plasmonic catalysis mediated by E-field-enhanced intramolecular metal-to-ligand charge transfer (MLCT) for direct photocatalysis of urea oxidation reaction (UOR). We evaluate the design of a hierarchical nanopigment architecture that incorporates 1.) a molecular photocatalyst, 2.) a spherical Ag NP as effective

metal-to-ligand charge transfer (MLCT) for direct photocatalysis of urea oxidation reaction (UOR). We evaluate the design of a hierarchical nanopigment architecture that incorporates 1.) a molecular photocatalyst, 2.) a spherical Ag NP as effective nanoantenna, and 3.) a lipid membrane layer as both scaffold and molecular spacer. The self-assembled lipid layer provides a facile and effective strategy to facilitate the localization of the photocatalyst at a separation between 2-4 nm from the Ag surface, which represents a "sweet spot" for plasmonic enhancement as it is close enough to the NP surface to provide high E-field intensity for the resonant enhancement of photoexcitation but sufficiently far away to limit the quenching of photoexcited states. As photocatalyst we chose trisbipyridine-Ruthenium(II), [Ru(bpy)₃]²⁺, which derives its photoreactivity from a light-mediated MLCT absorption²³⁻²⁴ that overlaps with the LSPR of the Ag NPs at around 430 nm. [Ru(bpy)₃]²⁺ and analogues play an important role in photoelectrochemical (PEC) conversions, either as photosensitizers, ²⁵⁻²⁷ or as photocatalysts in solar-to-fuel conversion. ²⁸⁻³⁰ The light harvesting efficiency of [Ru(bpy)₃]²⁺ is, however, fundamentally limited by the moderate extinction coefficient of its MLCT band (4,600-11,000 M¹cm¹), ³¹⁻³² which is much lower than those of high-performance dyes (> 200,000 M¹cm¹), ³³⁻³⁴ We test the





hypothesis that the E-field-mediated enhancement of the MLCT photoexcitation of [Ru(bpy)₃]²⁺ in plasmonic nanopigments can close this gap and achieve a measurable increase in photoreactivity. We implement a robust visible light fuel cell that achieves energy conversion through photo-oxidation of the ubiquitous waste molecule urea. To the best of our knowledge, our work presents the first example of a direct photocatalytic UOR as well as a first light-driven direct urea fuel cell (LDUFC).

RESULTS AND DISCUSSION

Assembly and Structural Characterization of Plasmonic Nanopigments

Artificial lipid membranes and micelles that mimic the hierarchical structure of biological photosynthetic systems have long been important components of man-made reactive and energy conversion systems.³⁵⁻³⁸ In our design of nanopigments, we utilize a self-assembled lipid membrane architecture around a Ag NP core to immobilize [Ru(bpy)₃]²⁺ in the near-field of the Ag NP. Lipidwrapping was achieved through modified one-pot synthesis³⁹⁻⁴² (See Supplemental Experimental Procedures). We adopt a lipid membrane composition based on simplified biological membrane model containing 45 mol % zwitterionic lipid DPPC (1,2dipalmitoyl-sn-glycero-3-phosphocholine), 5 mol % negatively-charged lipid DOPS (1,2-dioleoyl-sn-glycero-3-phospho-L-serine), 40 mol % lubricant molecule cholesterol, and 10 mol % [Ru(bpy₃)]²⁺. These lipids were tethered to the NP core through an intermediate octadecanethiol (ODT) layer that is chemisorbed to the Aq NP cores (Fig. 1A). In order to understand the equilibrium of [Ru(bpy₃)]²⁺ in the lipid membrane, we calculated the potential of mean force (PMF) of a [Ru(bpy₃)]²⁺ complex from a steered molecular dynamics simulation using Jarzynski's equality (Eq. S1)⁴³⁻⁴⁵ (Fig. 1B, see also supplemental experimental procedures). We first reconstructed an area of the nanopigments with Ag atoms, ODT, lipid layer and [Ru(bpy₃)]²⁺ at experimental proportions. [Ru(bpy₃)]²⁺ was allowed to equilibrate in the local lipid membrane environment. We then pulled the molecule along the cross-section of the lipid membrane to calculate the nonequilibrium work (W) as function of distance to the metal NPs surface. W is related to the equilibrium free energy difference (ΔF , PMF) using an exponential average (Eq. S1). The resulting PMF plot exhibits a minimum at around 2 nm, indicating a preferential localization of [Ru(bpy₃)]²⁺ close to the membrane surface at the interface formed by the hydrophilic lipid headgroups and the hydrophobic lipid tails.

We utilize Ag NP cores as effective nanoantennas. Due to their large polarizability⁴⁶ and optical cross-sections⁴⁷⁻⁴⁸ (absorption cross-section > $3x10^{-9}$ m², see Supplemental Experimental Procedures for calculations). Ag NPs can efficiently generate localized incident E-field intensity within a few nanometers of their surface⁴⁹⁻⁵⁰. We chose NPs with an average hydrodynamic diameter of





44.23±0.62 nm (from Dynamic Light Scattering, DLS), because NPs with much smaller diameters generate lower E-field intensities and suffer from higher dissipative losses,^{7, 49, 51-52} while larger NPs typically show retardation and high radiative losses.⁵³⁻⁵⁴ As expected, the LSPR absorbance spectrum of the Ag NP cores shows good spectral overlap with the [Ru(bpy)₃]²⁺ MLCT band at 415-450 nm (**Fig. 1C**).

To validate the successful nanopigment formation, we added small amounts of fluorescent lipid dye (Lissamine-Rhodamine-DSPE) into the lipid membrane and imaged the nanopigments with correlated darkfield and fluorescence microscopy (**Fig. 2A**). The optical colocalization of darkfield (top, NP cores) and fluorescence (middle, membrane) signals confirms a successful membrane assembly around the Ag NPs. We used Transmission Electron Microscopy (TEM) and High-Resolution TEM (HRTEM) to characterize the surface and membrane morphology of the plasmonic nanopigments. A uniform lipid membrane is clearly visible around the NP core in the TEM (**Fig. S1A**) and HRTEM (**Fig. 2B**) images. A statistical analysis of the thickness of the membrane for 70 particles showed an average membrane width of 3.8±1.4 nm, defining an upper boundary for the distance between [Ru(bpy₃)]²⁺ and Ag NP. In further proof of [Ru(bpy₃)]²⁺ binding, we mapped Ag and Ru across individual nanopigment particles using Energy Dispersive X-Ray Spectroscopy (EDX) under Scanning Transmission Electron Microscopy (STEM) mode. The resulting elemental maps confirm the co-existence of Ag (**Fig. 2D**) and Ru (**Fig. 2E**) within the boundary of the particle, providing additional experimental proof of a successful integration of [Ru(bpy₃)]²⁺.

Experimental Characterization of [Ru(bpy)₃]²⁺ Localization in the Lipid Membrane

Due to its amphiphilic nature, the nanopigment membrane provides both electrostatic and hydrophobic binding regions for [Ru(bpy₃)]²⁺. To probe the contributions of the two factors, we analyzed [Ru(bpy₃)]²⁺ binding to two control groups: (1.) nanocomposites with different surface charges but identical hydrophobic tail groups as for the nanopigments, and (2.) nanocomposites that lack the hydrophobic region but have similar surface charge as the nanopigments. (1.) was obtained by varying the amount of negatively-charged lipid DOPS or by replacing DOPS with cationic lipid EPC (1,2-dioleoyl-sn-glycero-3-ethylphosphocholine); (2.) was achieved by passivating Ag NPs cores with thiolated polyethylene glycol (PEG) with carboxyl end groups (HS-PEG-COOH, Mw=1000). The size, surface charge and amount of membrane-bound ¹⁰¹Ru is summarized in Fig. 2F, G. Before the incorporation of [Ru(bpy)₃]²⁺, the zeta potential of the liposomes becomes more negative with increasing amounts of DOPS, and more positive with increasing EPC. With increasing negative potential, we observe an overall increase in ¹⁰¹Ru concentration, indicating a contribution from Coulomb attraction in [Ru(bpy)₃]²⁺ binding. NPs without DOPS (0 mol %) deviate





from this overall trend. This group exhibits substantial aggregation due to the lack of interparticle electrostatic repulsion, and we attribute the high levels of ¹⁰¹Ru in this case to the inclusion of catalyst during agglomeration. Intriguingly, the PEG-passivated nanocomposite control shows a 48% decrease in ¹⁰¹Ru concentration in the absence of the hydrophobic tail group of the lipid layer relative to the nanopigments, despite having a similar zeta potential. These results are in good agreement with the membrane equilibrium simulations and PMT calculations in **Fig. 1A**, **B**, and indicate a structural model in which [Ru(bpy₃)]²⁺ is partially embedded in the membrane. COO⁻ anions from head groups of membrane DOPS pin the Ru(II) cationic center to the interface between hydrophic and hydrophilic membrane regions, while one or more bipyridine ligands are integrated into the membrane through hydrophobic interaction with lipid tail groups.

We varied the [Ru(bpy₃)]²⁺ input percentage in the liposomes used for nanopigment assembly to characterize the [Ru(bpy₃)]²⁺ loading capacity of the lipid layer (**Fig. S2**). Nanopigments with 10 mol % [Ru(bpy₃)]²⁺ demonstrated good binding efficacy and monodispersity, and is therefore used for the following analysis unless otherwise noted.

Plasmonic Enhancement of the Metal-to-Ligand Charge Transfer in Nanopigments

In order to quantify the effect of the plasmonic E-field enhancement on MLCT photoexcitation, we collected the UV-vis absorbance spectra of water suspensions of nanopigments and controls (Fig. 3A). The ¹⁰¹Ru (382 ppb) and ¹⁰⁷Ag (3937 ppb) concentrations were identical to the measured value in nanopigments in applicable groups. We calculated an extinction coefficient of 4230 M⁻¹cm⁻¹ for aqueous solution of [Ru(bpy₃)]²⁺ (orange, inset) at its MLCT absorbance maximum, which is in good agreement with previously reported values.³¹ Importantly, the nanopigments (red) exhibit a clear enhancement in absorbance in the MLCT range. We corrected the absorbance of the nanopigments for the contribution from the Ag NP by subtracting the absorbance of "bare" Ag colloid (black) at the absorbance maximum of 424 nm. The remaining absorbance, which corresponds to the E-field-enhanced MLCT band, is 35-fold higher than that of [Ru(bpy₃)]²⁺. The molar extinction coefficient of the MLCT band in the nanopigments reached 148,000 M⁻¹cm⁻¹, comparable to the benchmark of high performance dyes.³³⁻³⁴

For the control group with Au cores (green), no noticeable enhancement of the MLCT absorbance was observed; its spectrum only contains a peak at 540 nm, characteristic of the LSPR for 40 nm Au NPs. This stark contrast to nanopigments with Ag cores underlines that spectral overlap between the MLCT band and LSPR absorbance is essential for strong resonant enhancement. A simple mixture control of Ag NP colloid and [Ru(bpy₃)]²⁺ solution (blue) generated only a weak enhancement of the MLCT band. This finding corroborates that the preferential localization of the Ru(II) complex within the evanescent field of the NPs is a necessary factor for the plasmonic enhancement of MLCT.





The nanopigment architecture with the lipid membrane as molecular spacer effectively limits the reactivity loss of [Ru(bpy₃)]²⁺ through metal-associated pathways. To assess the extent of quenching on reactive photoexcited states, we measured the photoluminescence (PL) lifetime and quantum yield (QY) for an aqueous solution of [Ru(bpy₃)]²⁺ as well as for the nanopigments. The measured lifetime is determined by the phosphorescence of the Ru*(II) triplet state that is generated through rapid Intersystem Crossing (ISC) from the initial short-lived photo-excited singlet state.²⁴ The triplet state is sufficiently long-lived to allow reactive relaxation pathways and participate in charge or energy transfers (Fig. 3B). The measured PL lifetime of the aqueous suspensions of nanopigments was 371.7 ns (Fig. 3C), only slightly shorter than the 377.4 ns measured for [Ru(bpy)₃]²⁺ solution (Fig. 3D). The essentially identical lifetimes exclude a significant quenching of the excited state through the Ag NPs in the plasmonic nanopigments. We also performed lifetime measurements for [Ru(bpy)₃]²⁺ located closer to the metal NP. In this case, [Ru(bpy)₃]²⁺ were loaded onto Ag NPs functionalized with HS-PEG₃-COOH (Mw=238.3) (See Supplemental Experimental Procedures). The deprotonated carboxylic acid group of the short polymer localize [Ru(bpy)₃]²⁺ at a separation of around 1 nm⁵⁵-⁵⁶ from the Ag surfaces. Monoexponential fit of the emission tail reveal a PL lifetime of 2.35 ns for these samples, indicative of strong quenching (Fig. S3). QY measurements of the photoluminescence revealed a QY=4.55% for the plasmonic nanopigments compared with QY=1.95% for free $[Ru(bpy)_3]^{2+}$, and QY=0.02% for $[Ru(bpy)_3]^{2+}$ tethered by HS-PEG₃-COOH. We conclude that the lipid membrane around the Ag NPs in the nanopigments succeeds in positioning the [Ru(bpy3)]²⁺ photocatalyst in a "sweet spot" where substantial E-field enhancement of MLCT photoexcitation is achieved without strong quenching of the reactive excited state.

Characterizing Photoredox Reactivity and Stability of Nanopigments for Urea Oxidation Photocatalysis

We characterized the photoredox potentials of the nanopigments and the effects of plasmonic field enhancement on the photocatalysis with Linear Sweep Voltammetry (LSV) in a three-electrode setup (**Figure 4**). We drop-casted nanopigment suspensions and controls onto glassy carbon working electrodes and measured the current density in the voltage range of 0 - 1.2 V (vs. Ag/AgCl unless otherwise noted) with illumination from a focused 430 nm LED or in dark. During voltammetric measurements, the applied bias induces the oxidation of photogenerated Ru*(II) into Ru(III) (**Fig. 4A**), which is then available to facilitate oxidation processes.⁵⁷⁻⁵⁸

To assess the redox properties of the Ru species, we first used an electrolyte solution of 0.1 M NaOH + 0.01 M tripropylamine (TPrA), where the baseline is defined by water oxidation (**Fig. 4B**). TPrA is added as sacrificial reductant to rapidly reduce excessive Ru(III) to Ru*(II), which then replenishes steady state Ru(II) through radiative relaxation.⁵⁹ The LSV curve for 6





nanopigments with light (red) exhibits an early reaction onset ~350 mV as well as a drastic increase in photocurrent density relative to the dark curve (black), which confirms efficient photooxidation of water. The measurable oxidation peak at 650 mV in nanopigments with light can be assigned to the oxidation of the photogenerated Ru*(II) to Ru(III), and is therefore much less noticeable for both nanopigments in dark and the control group of lipid-wrapped Ag NPs with no [Ru(bpy)₃]²⁺ ("LipoAg"; +/- light: orange / blue). We also included a simple mixture control of Ag NPs colloid and [Ru(bpy)₃]²⁺ solution ("Mixture"; +/- light: purple/green) with identical concentrations as the nanopigments. The Ru*(II) oxidation peak is present in "Mixture" with illumination, but with a noticeably lower photocurrent density (J_{Photo}) than the nanopigments. To quantify the plasmonic enhancement, we compared the J_{Photo} associated with the Ru*(II) oxidation peak by subtracting the dark current density from that with light at 650 mV. We obtained a J_{Photo} as high as 7.03 mA/cm² for the nanopigments, with enhancement factors (EFs) of 5.3 and 59, respectively, relative to the "Mixture" and [Ru(bpy)₃]²⁺ controls (**Fig. 4B** inset).

Based on the favorable photooxidation potentials of photogenerated Ru*(II) and Ru(III) in the nanopigments, we next choose the urea oxidation reaction (UOR) as test system for the plasmonic catalysis. Urea (CO(NH₂)₂) is a common waste molecule from nitrogen cycles of mammals. Urea possesses high energy and hydrogen densities, 60 and great potentials in waste-to-energy conversions. In UOR, anodic urea oxidation (CO(NH₂)₂ + 6OH⁻ \rightarrow N₂ + 5H₂O + CO₂ + 6e⁻) is coupled to cathodic H₂ evolution in neutral or alkaline conditions (2H₂O + 2e⁻ \rightarrow H₂ + 2OH⁻), resulting in the overall reaction CO(NH₂)₂ + H₂O \rightarrow N₂ + 3H₂ + CO₂ $^{60\cdot62}$. Nickel-based oxides and hydroxides have received much attention as electrocatalysts to accelerate the sluggish 6-electron reaction of UOR. $^{60\cdot61}$, $^{63\cdot65}$ Although prior studies have demonstrated photosensitization of Ni UOR electrocatalysts by semiconductors, 64,66 direct photocatalysis of UOR has not been reported to the best of our knowledge.

We performed Linear Sweep voltammetry in an alkaline urea electrolyte with a human-urine equivalent 0.33 M urea in 0.1 M NaOH + 0.01 M TPrA ⁶³ (**Fig. 4C**). A sharp onset of current density for the nanopigments with light can be observed at 450 mV (red), leading to an extended oxidation plateau for Ru(III)-mediated urea oxidation. The shift of the reaction onset to lower voltages and the substantial increase in current density compared to nanopigments without illumination (black) confirm superb photocatalysis of UOR. We compared the J_{photo} associated with photogenerated Ru*(II)-Ru(III), which was determined to be 650 mV in **Fig. 4B** discussions. J_{photo} of the nanopigments is enhanced by factors of 5.4 and 50 relative to the "Mixture" and free [Ru(bpy₃)]²⁺ control, which are in good agreement with those obtained in NaOH+TPrA, indicating consistent and robust catalytic properties of the photogenerated Ru(III). Ru(III)-facilitated urea oxidation peaks at 750 mV, where we recorded a maximum J_{photo} of 56.0 mA/cm². This corresponds to an excellent Applied Bias Photon-to-Current Efficiency (ABPE) (**Eq. S4**) of 4.1%, comparable





to previously-reported state-of-the-art p-Si hydrogen evolution photocathodes $(2.9\%)^{67}$ and n-Si/NiO_x water oxidation photoanodes $(1.34\%)^{.68}$

In order to reflect photoelectrochemical kinetics and to relate the reaction rates and potentials, we construct Tafel Plots for nanopigments and control groups in both NaOH+TPrA (**Fig. 4D**) and alkaline urea electrolytes (**Fig. 4E**) (See Supplemental Experimental Procedures). A lower Tafel Slope typically indicates less potential input required for unit increase of current density, and hence better catalytic properties.⁶⁹ The illuminated nanopigments show the lowest Tafel slopes among all tested conditions. We calculate values of 188 mV/dec in NaOH+TPrA and 120 mV/dec alkaline urea electrolyte, close to the 120 mV/dec standard for high-surface-area photocatalysts.⁶⁸⁻⁶⁹

The scaffolding function of the lipid-wrapped architecture also contributes to promoting structural and photoelectrochemical stability of the $[Ru(bpy_3)]^{2+}$ photocatalyst. We evaluated the catalytic stability of nanopigments and of $[Ru(bpy_3)]^{2+}$ with chronoamperometry at 650 mV in alkaline urea electrolyte under constant illumination (**Fig. 4F**). Over an experimental duration of 6 h, J_{photo} remained much more stable at significantly higher values for nanopigments than for $[Ru(bpy)_3]^{2+}$. For the latter J_{photo} drastically decreased over the first 10 min of illumination due to photobleaching and depletion of steady state Ru(II).

Validation of E-Field-Enhanced Plasmonic Catalysis Mechanism

To elucidate the mechanisms of the enhanced UOR photocatalysis of nanopigments, we first investigated the effect of incident wavelength and power. As shown in Fig. 5A, *J*_{photo} in NaOH+TPrA and alkaline urea electrolytes generally follows the UV-vis absorbance spectrum of the nanopigments (red), with strong enhancement for incident wavelengths between 395 nm and 450 nm, which overlaps with the plasmon resonance of the nanopigments. Light power studies were carried out using a 430 nm LED (Fig. 5B) as well as a sunlight simulator (Fig. 5C) to better imitate the performance of the nanopigments in a solar cell. A linear dependency of *J*_{photo} on the incident power is obtained for both light sources. These data confirm that the observed increase in nanopigment photoreactivity is indeed related to the plasmon-enhanced optical absorption provided by the NPs.

Given the relative large size of the Ag NPs used in this work, we attribute the observed gain in photocatalysis primarily to the Effield-enhanced MLCT photoexcitation and not to hot charge carrier-associated processes. ⁵¹⁻⁵² To validate this assumption, we investigated the catalysis of nanocomposites in which the Ag sphere cores were replaced with triangular Ag nanoplates (Fig. 5D insets). The nanoplates sustain two LSPR modes respectively at 415 nm and 525 nm with similar dissipation. ⁴⁶ In both cases the decay of the plasmon could generate hot charge carriers but only the former mode has good spectral overlap with the [Ru(bpy)₃]²⁺ MLCT. After loading the lipid membrane with [Ru(bpy₃)]²⁺, the 415 nm band of Lipo-Ag Nanoplates-Ru nanocomposite control





is broadened by the MLCT of [Ru(bpy₃)]²⁺ while the 525 nm peak remains distinct (**Figure 5D**). We collected the LSV curves with illumination at either 430 nm or 565 nm to selectively excite the two LSPR modes. As shown in **Figure 5E** and **F**, J_{photo} is increased only for the mode that peaks at 415 nm close to the MLCT band but not for the plasmon mode at 525 nm, even though the latter mode has larger extinction. These results confirm that the enhanced photocatalysis of nanopigments derived from an E-field driven MLCT excitation enhancement mechanism.

Interestingly, the increase of J_{photo} for nanopigments over free [Ru(bpy₃)]²⁺ solution (EF = 50) is higher than the enhancement of absorbance (EF=35). We attribute the larger gain in photoreactivity to an additional photothermal effect sustained by Ag NP cores. We calculate a temperature increase of 2.89 K in the immediate vicinity of the nanopigments for the chosen experimental conditions (See Supplemental Experimental Procedures). Such increase in local temperature enhances the catalytic turnover and shifts the reaction towards products. We emphasize that the increase in local temperature of 2.89 K does not affect the structural stability of the nanopigments, as the temperature remains well below the glass transition temperatures of the membrane components (> 42 °C). 39

Implementation and Characterization of Visible Light-Driven Direct Urea Fuel Cell (LDUFC)

Achieving overall urea oxidation in a direct urea fuel cell (DUFC) has the exciting appeal of simultaneous energy conversion from an abundant source and waste water treatment. Based on the versatile redox properties of the nanopigments, we implemented a visible light-driven DUFC (LDUFC) in which nanopigments serve as both cathode and photoanode material. An electrolyte of 0.33 M Urea+0.1 M NaOH was used for characterizing the cell performance. We focused incident light onto the working electrode to generate photoexcited Ru*(II), which undergoes spontaneous oxidation at the photoanode (Ru*(II) - $e^- \rightarrow Ru(III)$). The cathode reaction Ru(II) + $e^- \rightarrow Ru(I)$ occurs on the non-illuminated "dark" electrode (**Fig. 6A**), giving an overall cell potential of +0.52 V.²³ The strong oxidizer Ru(III) facilitates urea oxidation at the photoanode, while Ru(I) reduces O₂ or CO₂ to re-generate Ru(II) at the cathode.

We monitored the Open Circuit Potential (OCP) of the LDUFC with illumination both from a 430 nm LED (**Fig. 6B**) and a sunlight simulator at 1-sun illumination (100 mW/cm²) (**Fig. 6C**) for proof-of-concept solar energy harvesting. We recorded the photovoltage, reflected by difference in OCP between light on and off stages, with alternating light on/off intervals of 150 s/350 s. The electrolyte was exchanged after 3 h to guarantee comparable kinetics in the reactions. For both illumination conditions the cell OCP stabilized after an initial decrease in magnitude and then performed steadily with photovoltages between 12 - 15 mV for more than 3 h. We recorded the cell short circuit current density using chronoamperometry with a same cell setup and





focused LED illumination. As shown in **Fig. 6D**, there is a consistent oscillation in photocurrent density centered at around 0.25 mA/cm². We attribute this oscillatory behavior to the photoelectrochemical cycling of the photoanode.⁷¹ Under continuous illumination, Ru(II) is rapidly consumed but more slowly replenished by the catalyzed 6-electron urea oxidation reaction, resulting in a consumption/replenishing cycle for the steady state population.

To further illuminate the nature of the electrode reactions, we purged the cell with nitrogen and recorded cell OCP under oxygen deficient conditions (**Fig. 6E**). In the beginning of the measurement, after an activation stage in the first 10 min, the photovoltage show an initial increase in magnitude. Subsequent addition of air triggered a measurable increase in the light response. Overall, lower OCP values are observed with nitrogen purging. These observations are consistent with our model of LDUFC reactions in which O₂ and CO₂ are reduced at the cathode. In the absence of O₂, an increasing amount of CO₂ generated through the anode photoreaction of urea oxidation dominates the cathode reaction in a self-accelerating manner. When O₂ becomes available, the reaction rate at the cathode increases, resulting in an overall increase of OCP as well as a stronger light-induced modulation of OCP.

In summary, we have demonstrated efficient plasmonic E-field enhancement of [Ru(bpy)₃]²⁺-mediated photocatalytic urea oxidation in a hierarchical nanopigment architecture. The nanopigments contain a lipid layer self-assembled around a ~45 nm Ag nanoantenna with favorable spectral overlap between the Ag NPs LSPR and [Ru(bpy)₃]²⁺ MLCT. Our experimental and theoretical analyses suggest that the amphiphilic nature of the self-assembled membrane facilitates both electrostatic and hydrophobic interaction with [Ru(bpy)₃]²⁺ to achieve localization of the photocatalyst at an electromagnetic "sweet spot" approximately 2 – 4 nm from the metal surface. At the "sweet spot", strong E-field intensity provides substantial enhancement of photocatalyst excitation, but quenching of the excited reactive states in the photocatalyst through the metal is limited. The nanopigments achieved efficient direct photocatalysis of urea oxidation, with photocurrent densities more than 50 times higher than for [Ru(bpy)₃]²⁺ and an excellent photoelectrode efficiency of 4.1%. We also implemented a first Visible Light-Driven Direct Urea Fuel Cell (LDUFC) with LED and sunlight simulator, and demonstrated steady on/off photovoltaic performance and OCPs for over 4 hours. Our proof-of-principle implementations of UOR and LDUFC promises great achievements in solar energy conversion and waste water treatment. Future efforts focusing on expanding the spectrum of reactions catalyzed by photocatalytic nanopigments containing [Ru(bpy)₃]²⁺ or other transition metal complexes will clarify the full potential of the approach and may lead to entirely new classes of plasmon-enhanced biomimetic nanoreactors.





EXPERIMENTAL PROCEDURES

Detailed experimental procedures is included in Supplemental Experimental Procedures.

DATA AND SOFTWARE AVAILABILITY

All relevant data are available from the authors upon request.

SUPPLEMENTAL INFORMATION

Supplemental Information includes Supplemental Experimental Procedures, four supplemental figures and two supplemental tables.

- Figure S1. Structural Characterizations of the Nanopigments.
- Table S1. Characterizations of Nanopigments with Varying Input Percentages of [Ru(bpy)₃]²⁺.
- $\textbf{Figure S2}. \ \ Characterizations \ of \ Nanopigments \ with \ Varying \ Input \ Percentages \ of \ [Ru(bpy)_3]^{2+}.$
- Table S2. Characterizations of [Ru(bpy)₃]²⁺ Binding in the Nanopigments.
- Figure S3. Photophysical Characterizations.
- Figure S4. Electrochemical Characterizations for Plasmonic Enhancement Mechanism.

ACKNOWLEDGMENTS

This work was partially supported by the National Science Foundation through grants CHE-1609778 and CHE-1808241. The authors thank Prof. Chen Yang and Dr. Melissa Cardona for discussions of electrochemical characterizations, and Prof. Allison Dennis for access to the luminescence lifetime spectrometer.

AUTHOR CONTRIBUTIONS

contributed to the final manuscript.

X.A. designed and conducted the experiments, D.S. designed and conducted the membrane molecular dynamics simulations,

T.K. supervised the simulations, B.M.R. conceived the idea and supervised the experiments; all authors discussed the results and

11





DECLARATION OF INTERESTS

B.M.R. has filed a patent for GM3-functionalized nanoparticles, which contain a lipid-wrapped nanoparticle core.

REFERENCES AND NOTES

- 1. Kale, M. J.; Avanesian, T.; Christopher, P., Direct photocatalysis by plasmonic nanostructures. Acs Catalysis 2013, 4 (1), 116-128.
- 2. Wang, C.; Astruc, D., Nanogold plasmonic photocatalysis for organic synthesis and clean energy conversion. *Chem Soc Rev* **2014**, 43 (20), 7188-216.
- 3. Verma, P.; Kuwahara, Y.; Mori, K.; Yamashita, H., Pd/Ag and Pd/Au bimetallic nanocatalysts on mesoporous silica for plasmon-mediated enhanced catalytic activity under visible light irradiation. *Journal of Materials Chemistry A* **2016**, 4 (26), 10142-10150.
- 4. Ingram, D. B.; Linic, S., Water splitting on composite plasmonic-metal/semiconductor photoelectrodes: evidence for selective plasmon-induced formation of charge carriers near the semiconductor surface. *Journal of the American Chemical Society* **2011**, *133* (14), 5202-5205.
- 5. Mubeen, S.; Hernandez-Sosa, G.; Moses, D.; Lee, J.; Moskovits, M., Plasmonic photosensitization of a wide band gap semiconductor: converting plasmons to charge carriers. *Nano letters* **2011**, *11* (12), 5548-5552.
- 6. Li, J.; Cushing, S. K.; Zheng, P.; Senty, T.; Meng, F.; Bristow, A. D.; Manivannan, A.; Wu, N., Solar hydrogen generation by a CdS-Au-TiO2 sandwich nanorod array enhanced with Au nanoparticle as electron relay and plasmonic photosensitizer. *Journal of the American Chemical Society* **2014,** *136* (23), 8438-8449.
- 7. Zhang, Y.; He, S.; Guo, W.; Hu, Y.; Huang, J.; Mulcahy, J. R.; Wei, W. D., Surface-plasmon-driven hot electron photochemistry. *Chemical reviews* **2017**, 118 (6), 2927-2954.
- 8. Reineck, P.; Lee, G. P.; Brick, D.; Karg, M.; Mulvaney, P.; Bach, U., A solid-state plasmonic solar cell via metal nanoparticle self-assembly. Advanced Materials 2012, 24 (35), 4750-4755.
- 9. Mori, K.; Kawashima, M.; Che, M.; Yamashita, H., Enhancement of the photoinduced oxidation activity of a ruthenium(II) complex anchored on silica-coated silver nanoparticles by localized surface plasmon resonance. *Angew Chem Int Ed Engl* **2010**, *49* (46), 8598-601.
- 10. Choi, K. M.; Kim, D.; Rungtaweevoranit, B.; Trickett, C. A.; Barmanbek, J. T.; Alshammari, A. S.; Yang, P.; Yaghi, O. M., Plasmon-Enhanced Photocatalytic CO(2) Conversion within Metal-Organic Frameworks under Visible Light. *J Am Chem Soc* **2017**, *139* (1), 356-362.
- 11. Li, J.; Cushing, S. K.; Bright, J.; Meng, F.; Senty, T. R.; Zheng, P.; Bristow, A. D.; Wu, N., Ag@ Cu2O core-shell nanoparticles as visible-light plasmonic photocatalysts. Acs Catalysis 2012, 3 (1), 47-51.
- 12. Cushing, S. K.; Li, J.; Meng, F.; Senty, T. R.; Suri, S.; Zhi, M.; Li, M.; Bristow, A. D.; Wu, N., Photocatalytic activity enhanced by plasmonic resonant energy transfer from metal to semiconductor. *Journal of the American Chemical Society* **2012**, *134* (36), 15033-15041.
- 13. Linic, S.; Christopher, P.; Ingram, D. B., Plasmonic-metal nanostructures for efficient conversion of solar to chemical energy. *Nature materials* **2011,** *10* (12), 911.
- 14. Christopher, P.; Ingram, D. B.; Linic, S., Enhancing photochemical activity of semiconductor nanoparticles with optically active Ag nanostructures: photochemistry mediated by Ag surface plasmons. *The Journal of Physical Chemistry C* **2010**, 114 (19), 9173-9177.
- 15. Hou, W.; Cronin, S. B., A Review of Surface Plasmon Resonance-Enhanced Photocatalysis. *Advanced Functional Materials* **2013**, *23* (13), 1612-1619.
- 16. Lin, X.; Jumabekov, A. N.; Lal, N. N.; Pascoe, A. R.; Gómez, D. E.; Duffy, N. W.; Chesman, A. S.; Sears, K.; Fournier, M.; Zhang, Y., Dipole-field-assisted charge extraction in metal-perovskite-metal back-contact solar cells. *Nature communications* **2017**, *8* (1), 613.
- 17. Gandra, N.; Portz, C.; Tian, L.; Tang, R.; Xu, B.; Achilefu, S.; Singamaneni, S., Probing Distance-Dependent Plasmon-Enhanced Near-Infrared Fluorescence Using Polyelectrolyte Multilayers as Dielectric Spacers. *Angewandte Chemie* **2014**, *126* (3), 885-889.
- 18. Jain, P. K.; Huang, W.; El-Sayed, M. A., On the universal scaling behavior of the distance decay of plasmon coupling in metal nanoparticle pairs: a plasmon ruler equation. *Nano Letters* **2007**, *7* (7), 2080-2088.
- 19. Shanthil, M.; Thomas, R.; Swathi, R.; George Thomas, K., Ag@ SiO2 core–shell nanostructures: distance-dependent plasmon coupling and SERS investigation. The journal of physical chemistry letters 2012, 3 (11), 1459-1464.
- 20. Huang, T.; Murray, R. W., Quenching of [Ru (bpy) 3] 2+ fluorescence by binding to Au nanoparticles. Langmuir 2002, 18 (18), 7077-7081.
- 21. Anger, P.; Bharadwaj, P.; Novotny, L., Enhancement and quenching of single-molecule fluorescence. Physical review letters 2006, 96 (11), 113002.
- 22. Kedem, O.; Wohlleben, W.; Rubinstein, I., Distance-dependent fluorescence of tris (bipyridine) ruthenium (II) on supported plasmonic gold nanoparticle ensembles. *Nanoscale* **2014**, *6* (24), 15134-15143.
- 23. Prier, C. K.; Rankic, D. A.; MacMillan, D. W., Visible light photoredox catalysis with transition metal complexes: applications in organic synthesis. *Chem Rev* 2013, 113 (7), 5322-63.
- 24. Sanchez-Murcia, P. A.; Nogueira, J. J.; Gonzalez, L., Exciton Localization on Ru-Based Photosensitizers Induced by Binding to Lipid Membranes. *J Phys Chem Lett* **2018**, *9* (4), 683-688.
- 25. Shimakoshi, H.; Nishi, M.; Tanaka, A.; Chikama, K.; Hisaeda, Y., Photocatalytic function of a polymer-supported B12 complex with a ruthenium trisbipyridine photosensitizer. *Chem Commun (Camb)* **2011**, *47* (23), 6548-50.
- 26. Castellano, F. N.; McCusker, C. E., MLCT sensitizers in photochemical upconversion: past, present, and potential future directions. *Dalton Transactions* **2015**, 44 (41), 17906-17910.





- 27. Srivastava, R., On the viability of ruthenium (II) N-heterocyclic carbene complexes as dye-sensitized solar cell (DSSCs): A theoretical study. Computational and Theoretical Chemistry 2014, 1045, 47-56.
- 28. Lin, S.; Ischay, M. A.; Fry, C. G.; Yoon, T. P., Radical cation Diels-Alder cycloadditions by visible light photocatalysis. *J Am Chem Soc* **2011**, *133* (48), 19350-3.
- 29. Sala, X.; Ertem, M. Z.; Vigara, L.; Todorova, T. K.; Chen, W.; Rocha, R. C.; Aquilante, F.; Cramer, C. J.; Gagliardi, L.; Llobet, A., The cis-[Ru(II)(bpy)2(H2O)2]2+ water-oxidation catalyst revisited. *Angew Chem Int Ed Engl* **2010**, 49 (42), 7745-7.
- 30. Burian, M.; Syrgiannis, Z.; La Ganga, G.; Puntoriero, F.; Natali, M.; Scandola, F.; Campagna, S.; Prato, M.; Bonchio, M.; Amenitsch, H., Ruthenium based photosensitizer/catalyst supramolecular architectures in light driven water oxidation. *Inorganica chimica acta* 2017, 454, 171-175.
- 31. Muller, P.; Brettel, K., [Ru(bpy)(3)](2+) as a reference in transient absorption spectroscopy: differential absorption coefficients for formation of the long-lived (3)MLCT excited state. *Photochem Photobiol Sci* **2012**, *11* (4), 632-6.
- 32. Yoshimura, A.; Hoffman, M. Z.; Sun, H., An evaluation of the excited state absorption spectrum of Ru (bpy) 32+ in aqueous and acetonitrile solutions. *Journal of Photochemistry and Photobiology A: Chemistry* 1993, 70 (1), 29-33.
- 33. Chen, F.; Zhao, J.; Hidaka, H., Highly selective deethylation of rhodamine B: Adsorption and photooxidation pathways of the dye on the TiO2/SiO2 composite photocatalyst. *International Journal of Photoenergy* **2003**, 5 (4), 209-217.
- 34. Mujumdar, R. B.; Ernst, L. A.; Mujumdar, S. R.; Lewis, C. J.; Waggoner, A. S., Cyanine dye labeling reagents: sulfoindocyanine succinimidyl esters. *Bioconjugate chemistry* **1993**, 4 (2), 105-111.
- 35. Calvin, M., Simulating Photosynthetic Quantum Conversion. Acc. Chem. Res. 1978, 10, 369-374.
- 36. Elani, Y.; Trantidou, T.; Wylie, D.; Dekker, L.; Polizzi, K.; Law, R. V.; Ces, O., Constructing vesicle-based artificial cells with embedded living cells as organelle-like modules. Sci Rep 2018, 8 (1), 4564.
- 37. Noireaux, V.; Libchaber, A., A vesicle bioreactor as a step toward an artificial cell assembly. *Proceedings of the National Academy of Sciences* **2004,** 101 (51), 17669-17674.
- 38. Olenick, L. L.; Troiano, J. M.; Vartanian, A.; Melby, E. S.; Mensch, A. C.; Zhang, L.; Hong, J.; Mesele, O.; Qiu, T.; Bozich, J., Lipid Corona Formation from Nanoparticle Interactions with Bilayers. Chem 2018, 4 (11), 2709-2723.
- 39. Xu, F.; Reiser, M.; Yu, X.; Gummuluru, S.; Wetzler, L.; Reinhard, B. M., Lipid Mediated Targeting with Membrane-Wrapped Nanoparticles in the Presence of Corona Formation. ACS Nano 2015. 10. 1189-1200.
- 40. Yu, X.; Feizpour, A.; Ramirez, N.-G. P.; Wu, L.; Akiyama, H.; Yu, X.; Gummuluru, S.; Reinhard, B. M., Glycosphingolipid-functionalized nanoparticles recapitulate CD169-dependent HIV-1 uptake and trafficking in dendritic cells. *Nature Communications* **2014**, *5*, 4136.
- 41. Xu, F.; Bandara, A.; Akiyama, H.; Eshaghi, B.; Stelter, D.; Keyes, T.; Straub, J. E.; Gummuluru, S.; Reinhard, B. M., Membrane-wrapped nanoparticles probe divergent roles of GM3 and phosphatidylserine in lipid-mediated viral entry pathways. *Proceedings of the National Academy of Sciences* 2018, 115 (39), E9041-E9050.
- 42. Yu, X.; Xu, F.; Ramirez, N.-G. P.; Kijewski, S. D.; Akiyama, H.; Gummuluru, S.; Reinhard, B. r. M., Dressing up nanoparticles: A membrane wrap to induce formation of the virological synapse. ACS nano 2015, 9 (4), 4182-4192.
- 43. Ozer, G.; Valeev, E. F.; Quirk, S.; Hernandez, R., Adaptive steered molecular dynamics of the long-distance unfolding of neuropeptide y. *Journal of chemical theory and computation* **2010**, *6* (10), 3026-3038.
- 44. Jarzynski, C., Nonequilibrium equality for free energy differences. *Physical Review Letters* **1997,** 78 (14), 2690.
- 45. Park, S.; Schulten, K., Calculating potentials of mean force from steered molecular dynamics simulations. *The Journal of chemical physics* **2004**, 120 (13), 5946-5961.
- 46. Gaspar, D.; Pimentel, A.; Mendes, M.; Mateus, T.; Falcão, B.; Leitão, J.; Soares, J.; Araújo, A.; Vicente, A.; Filonovich, S., Ag and Sn nanoparticles to enhance the near-infrared absorbance of a-Si: H thin films. *Plasmonics* **2014**, *9* (5), 1015-1023.
- 47. Hlaing, M.; Gebear-Eigzabher, B.; Roa, A.; Marcano, A.; Radu, D.; Lai, C.-Y., Absorption and scattering cross-section extinction values of silver nanoparticles. *Optical Materials* **2016**, *58*, 439-444.
- 48. Yguerabide, J.; Yguerabide, E. E., Light-scattering submicroscopic particles as highly fluorescent analogs and their use as tracer labels in clinical and biological applications: II. Experimental characterization. *Analytical biochemistry* **1998**, *262* (2), 157-176.
- 49. Kelly, K. L.; Coronado, E.; Zhao, L. L.; Schatz, G. C., The optical properties of metal nanoparticles: The influence of size, shape, and dielectric environment. *J Phys Chem B* **2003**, 107 (3), 668-677.
- 50. Aslam, U.; Rao, V. G.; Chavez, S.; Linic, S., Catalytic conversion of solar to chemical energy on plasmonic metal nanostructures. *Nature Catalysis* **2018**, 1 (9), 656.
- 51. Manjavacas, A.; Liu, J. G.; Kulkarni, V.; Nordlander, P., Plasmon-induced hot carriers in metallic nanoparticles. ACS nano 2014, 8 (8), 7630-7638.
- 52. Reineck, P.; Brick, D.; Mulvaney, P.; Bach, U., Plasmonic hot electron solar cells: the effect of nanoparticle size on quantum efficiency. *The journal of physical chemistry letters* **2016**, *7* (20), 4137-4141.
- 53. Ringe, E.; McMahon, J. M.; Sohn, K.; Cobley, C.; Xia, Y.; Huang, J.; Schatz, G. C.; Marks, L. D.; Van Duyne, R. P., Unraveling the effects of size, composition, and substrate on the localized surface plasmon resonance frequencies of gold and silver nanocubes: a systematic single-particle approach. *The Journal of Physical Chemistry C* 2010, 114 (29), 12511-12516.
- 54. Bharadwaj, P.; Novotny, L., Spectral dependence of single molecule fluorescence enhancement. Optics Express 2007, 15 (21), 14266-14274.
- 55. Ma, Z.; LeBard, D. N.; Loverde, S. M.; Sharp, K. A.; Klein, M. L.; Discher, D. E.; Finkel, T. H., TCR triggering by pMHC ligands tethered on surfaces via poly (ethylene glycol) depends on polymer length. *PloS one* **2014**, *9* (11), e112292.
- 56. Hill, R. T.; Mock, J. J.; Hucknall, A.; Wolter, S. D.; Jokerst, N. M.; Smith, D. R.; Chilkoti, A., Plasmon ruler with angstrom length resolution. ACS nano 2012, 6 (10), 9237-9246.
- 57. Volpato, G. A.; Bonetto, A.; Marcomini, A.; Mialane, P.; Bonchio, M.; Natali, M.; Sartorel, A., Proton coupled electron transfer from Co3O4 nanoparticles to photogenerated Ru (bpy) 33+: base catalysis and buffer effect. Sustainable Energy & Fuels 2018, 2 (9), 1951-1956.
- 58. Bazzan, I.; Volpe, A.; Dolbecq, A.; Natali, M.; Sartorel, A.; Mialane, P.; Bonchio, M., Cobalt based water oxidation catalysis with photogenerated Ru (bpy) 33+: Different kinetics and competent species starting from a molecular polyoxometalate and metal oxide nanoparticles capped with a bisphosphonate alendronate pendant. Catalysis Today 2017, 290, 39-50.





- 59. Kerr, E.; Doeven, E. H.; Wilson, D. J.; Hogan, C. F.; Francis, P. S., Considering the chemical energy requirements of the tri-n-propylamine coreactant pathways for the judicious design of new electrogenerated chemiluminescence detection systems. *Analyst* 2016, 141 (1), 62-9.
- 60. Boggs, B. K.; King, R. L.; Botte, G. G., Urea electrolysis: direct hydrogen production from urine. Chem Commun (Camb) 2009, (32), 4859-61.
- 61. Vedharathinam, V.; Botte, G. G., Understanding the electro-catalytic oxidation mechanism of urea on nickel electrodes in alkaline medium. *Electrochimica Acta* **2012**, *81*, 292-300.
- 62. Chen, S.; Duan, J.; Vasileff, A.; Qiao, S. Z., Size Fractionation of Two-Dimensional Sub-Nanometer Thin Manganese Dioxide Crystals towards Superior Urea Electrocatalytic Conversion. *Angewandte Chemie International Edition* **2016**, *5*5 (11), 3804-3808.
- 63. Zhu, X.; Dou, X.; Dai, J.; An, X.; Guo, Y.; Zhang, L.; Tao, S.; Zhao, J.; Chu, W.; Zeng, X. C.; Wu, C.; Xie, Y., Metallic Nickel Hydroxide Nanosheets Give Superior Electrocatalytic Oxidation of Urea for Fuel Cells. *Angew Chem Int Ed Engl* **2016**, 55 (40), 12465-9.
- 64. Xu, D.; Fu, Z.; Wang, D.; Lin, Y.; Sun, Y.; Meng, D.; Feng Xie, T., A Ni(OH)2-modified Ti-doped alpha-Fe2O3 photoanode for improved photoelectrochemical oxidation of urea: the role of Ni(OH)2 as a cocatalyst. *Phys Chem Chem Phys* **2015**, 17 (37), 23924-30.
- 65. Tong, Y.; Chen, P.; Zhang, M.; Zhou, T.; Zhang, L.; Chu, W.; Wu, C.; Xie, Y., Oxygen vacancies confined in nickel molybdenum oxide porous nanosheets for promoted electrocatalytic urea oxidation. Acs Catalysis 2017, 8 (1), 1-7.
- 66. Wang, G.; Ling, Y.; Lu, X.; Wang, H.; Qian, F.; Tong, Y.; Li, Y., Solar driven hydrogen releasing from urea and human urine. *Energy & Environmental Science* **2012**, *5* (8).
- 67. Esposito, D. V.; Levin, I.; Moffat, T. P.; Talin, A. A., H 2 evolution at Si-based metal-insulator-semiconductor photoelectrodes enhanced by inversion channel charge collection and H spillover. *Nature Materials* **2013**, *12* (6), 562.
- 68. Sun, K.; Park, N.; Sun, Z.; Zhou, J.; Wang, J.; Pang, X.; Shen, S.; Noh, S. Y.; Jing, Y.; Jin, S., Nickel oxide functionalized silicon for efficient photo-oxidation of water. Energy & Environmental Science 2012, 5 (7), 7872-7877.
- 69. Walter, M. G.; Warren, E. L.; McKone, J. R.; Boettcher, S. W.; Mi, Q.; Santori, E. A.; Lewis, N. S., Solar water splitting cells. *Chemical reviews* **2010**, 110 (11), 6446-6473.
- 70. Yu, Y.; Sundaresan, V.; Willets, K. A., Hot carriers versus thermal effects: Resolving the enhancement mechanisms for plasmon-mediated photoelectrochemical reactions. *The Journal of Physical Chemistry C* **2018**, *122* (9), 5040-5048.
- 71. You, S.; Gong, X.; Wang, W.; Qi, D.; Wang, X.; Chen, X.; Ren, N., Enhanced Cathodic Oxygen Reduction and Power Production of Microbial Fuel Cell Based on Noble-Metal-Free Electrocatalyst Derived from Metal-Organic Frameworks. *Advanced Energy Materials* **2016**, *6* (1), 1501497.

Figure and Scheme Titles and Legends



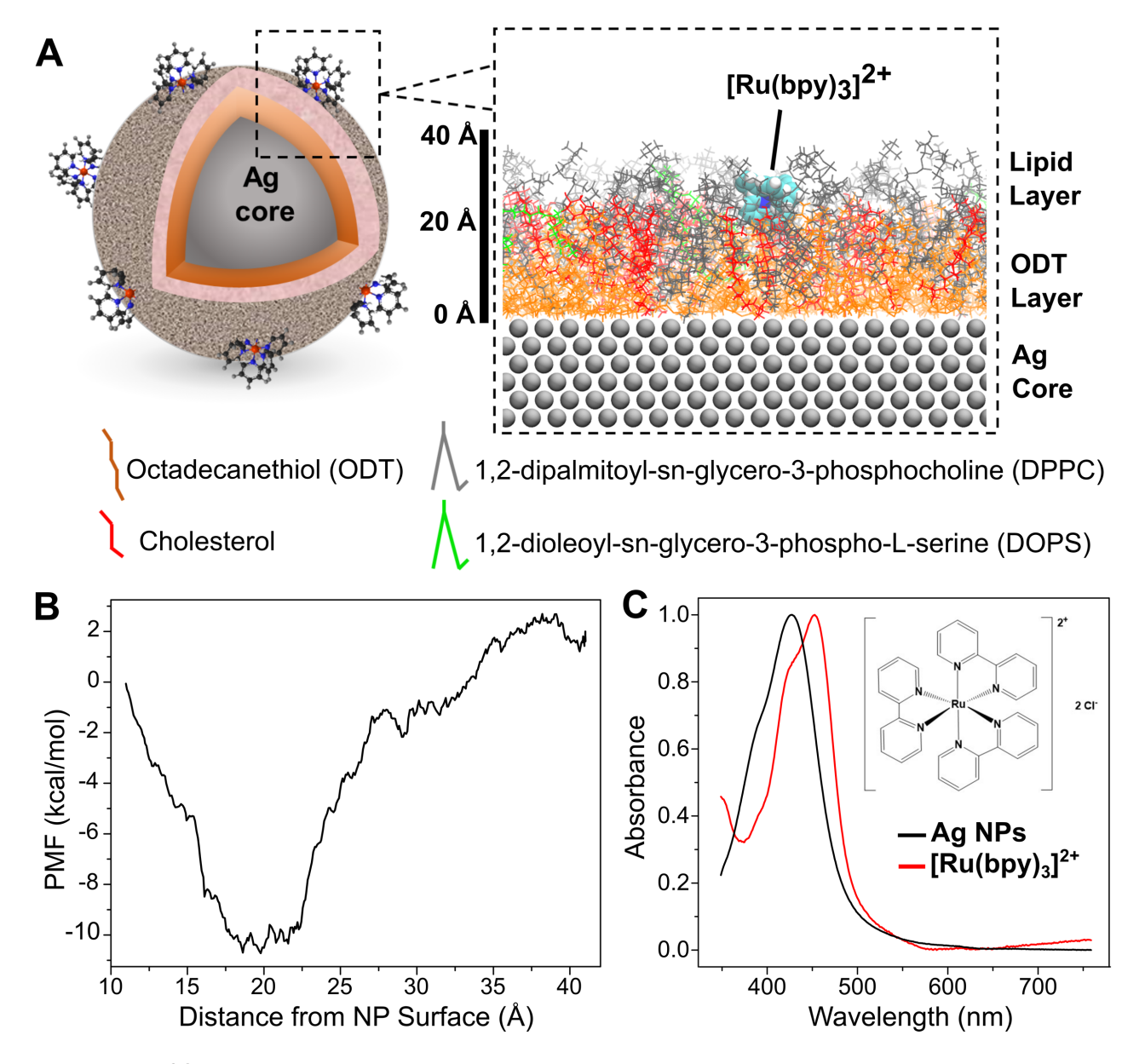


Figure 1. Design of the Nanopigment.

(A) Scheme for the nanopigment hierarchical structure; zoomed in: simulated surface morphology diagram of the nanopigment. Water molecules are not shown in the diagram.

(B) Plot of potential of mean force (PMF) of [Ru(bpy)₃]²⁺ molecule over lipid membrane cross-sectional distance from NP surface.

(C) Normalized UV-vis absorbance spectra of 44 nm Ag NP colloid and [Ru(bpy)₃]²⁺ water solution; inset: molecular structure of [Ru(bpy)₃]Cl₂.

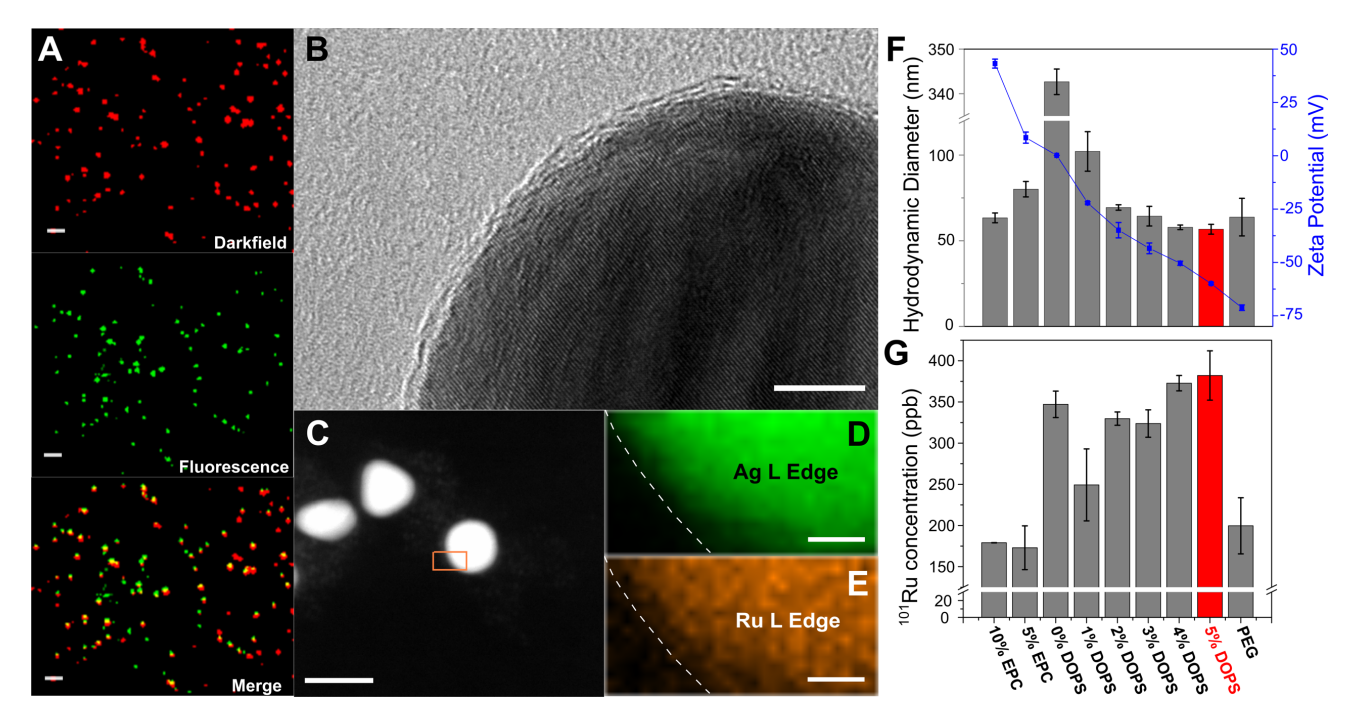


Figure 2. Structural Characterizations of the Nanopigments.

- (A) Darkfield image (Top), fluorescence image (middle) and merge (bottom) of an area with nanopigments under inverted microscope; scale bars=1 µm. (B) HRTEM image of a nanopigment particle, scale bar=10 nm. See also **Fig. S1**.
- (C) STEM image of nanopigments with scan area (orange rectangle) for EDX element mapping scans, scale bar=50 nm.
- (D and E) EDX elemental scan maps with (D) Ag L Edge and (E) Ru L Edge; scale bars=5 nm.
- (F) DLS results of hydrodynamic diameters of nanopigments and nanocomposite controls (Columns), and Zeta potentials of corresponding liposomes before incorporation of [Ru(bpy)₃]²⁺ (scattered plot). Error bars are standard deviations of three measurements.
- (G) Inductively Coupled Plasma Mass Spectrometry (ICP-MS) results of incorporated ¹⁰¹Ru concentrations of nanopigments and nanocomposite controls. Error bars are standard deviations of three measurements. (F and G) All percentages are mol %, the group with 5% DOPS represents standard nanopigment composition (red).



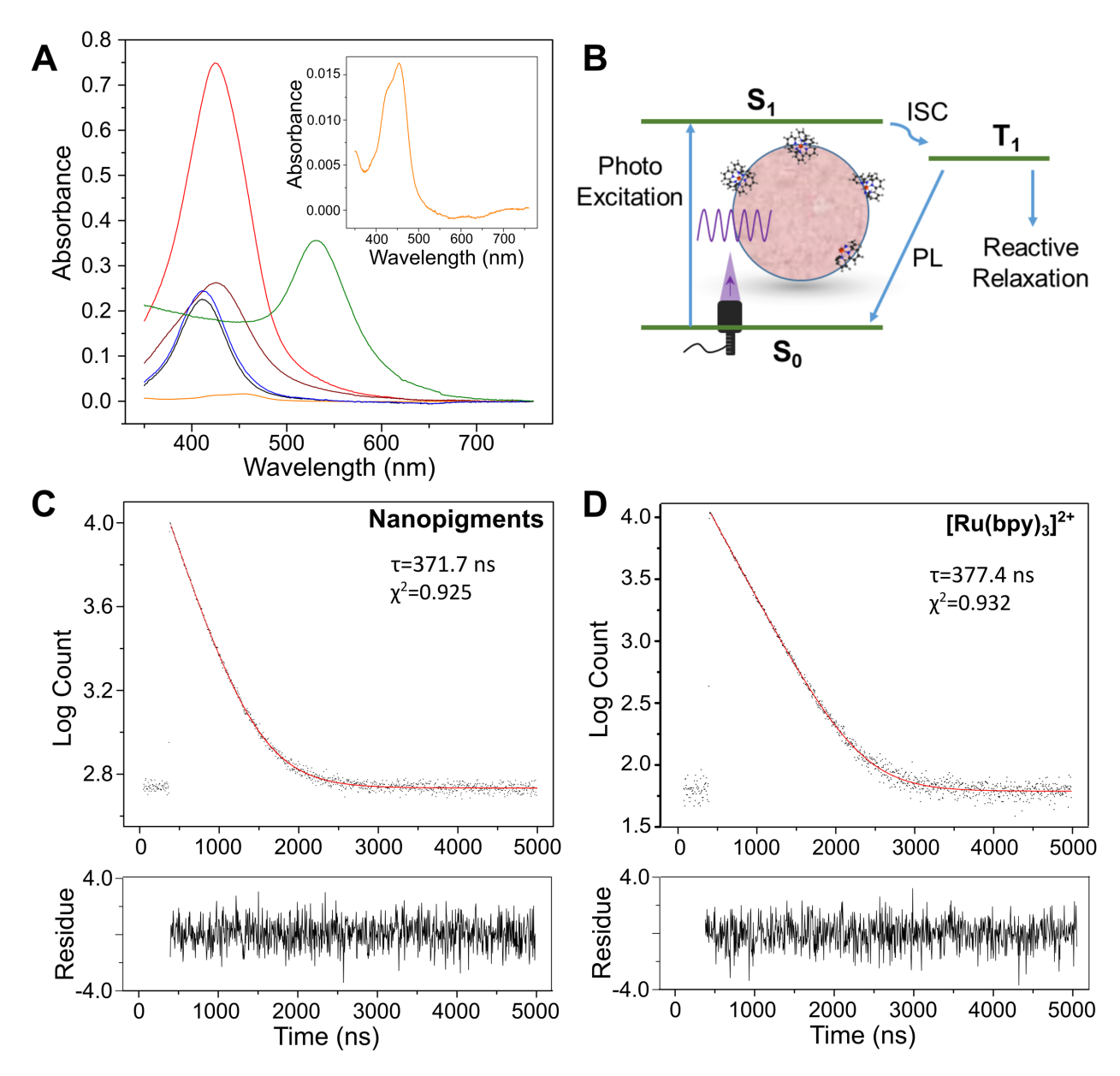


Figure 3. Photophysical Characterizations.

(A) UV-vis absorbance spectra of nanopigment colloid (red); "bare" Ag NPs (black); membrane wrapped Ag NPs without photocatalyst (LipoAg, brown); aqueous solution of [Ru(bpy)₃]²⁺ (orange, inset); mixture of Ag NPs and aqueous [Ru(bpy)₃]²⁺ solution (blue); and control nanopigments with Au NP cores (green). (B) Scheme for the photoexcitation and interstate transitions of [Ru(bpy)₃]²⁺.

(C and D) Photoluminescence decay patterns and monoexponential fit curves (red) for (C) nanopigments and (D) $[Ru(bpy)_3]^{2+}$ water solution.

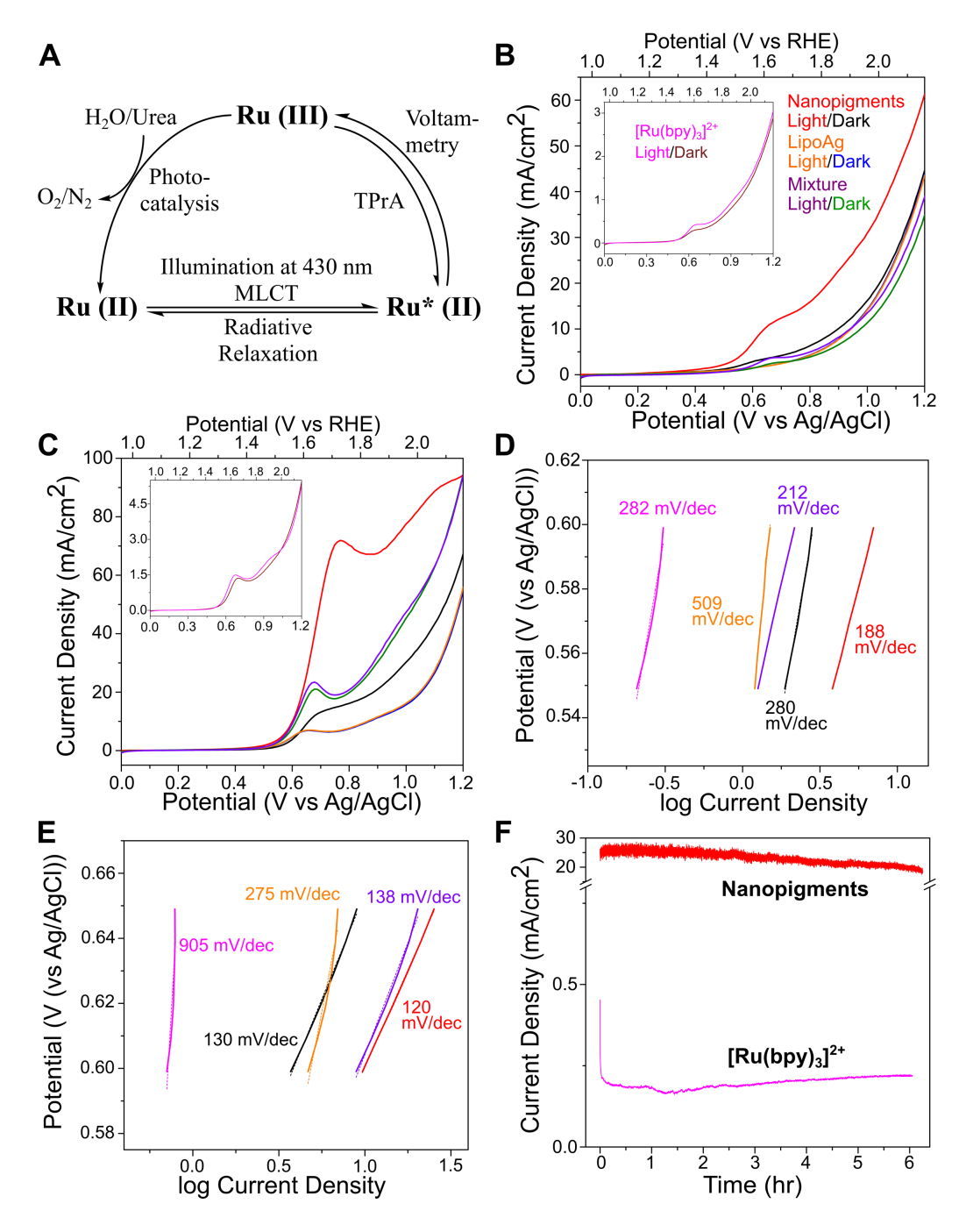


Figure 4. Electrochemical Characterizations.

(A) Scheme for the photocatalytic reaction mechanism of nanopigments in voltammetric measurements.

(B and C) Linear Sweep Voltammetry curves in (B) 0.1 M NaOH+0.01 M TPrA and (C) alkaline urea electrolyte.

(D and E) Tafel plots in (D) 0.1 M NaOH+0.01 M TPrA and (E) alkaline urea electrolyte.

(F) Chronoamperometry curves for nanopigments (Red) and just $[Ru(bpy)_3]^{2+}$ (magenta) in alkaline urea electrolyte under 430 nm LED illumination and with 750 mV potential.

Color code in (B-F): Nanopigments +/- light: Red/Black; LipoAg +/- light: Orange/Blue; "Mixture" control +/- light: Purple/Green; $[Ru(bpy)_3]^{2+}$ +/- light: Magenta/Wine (insets).

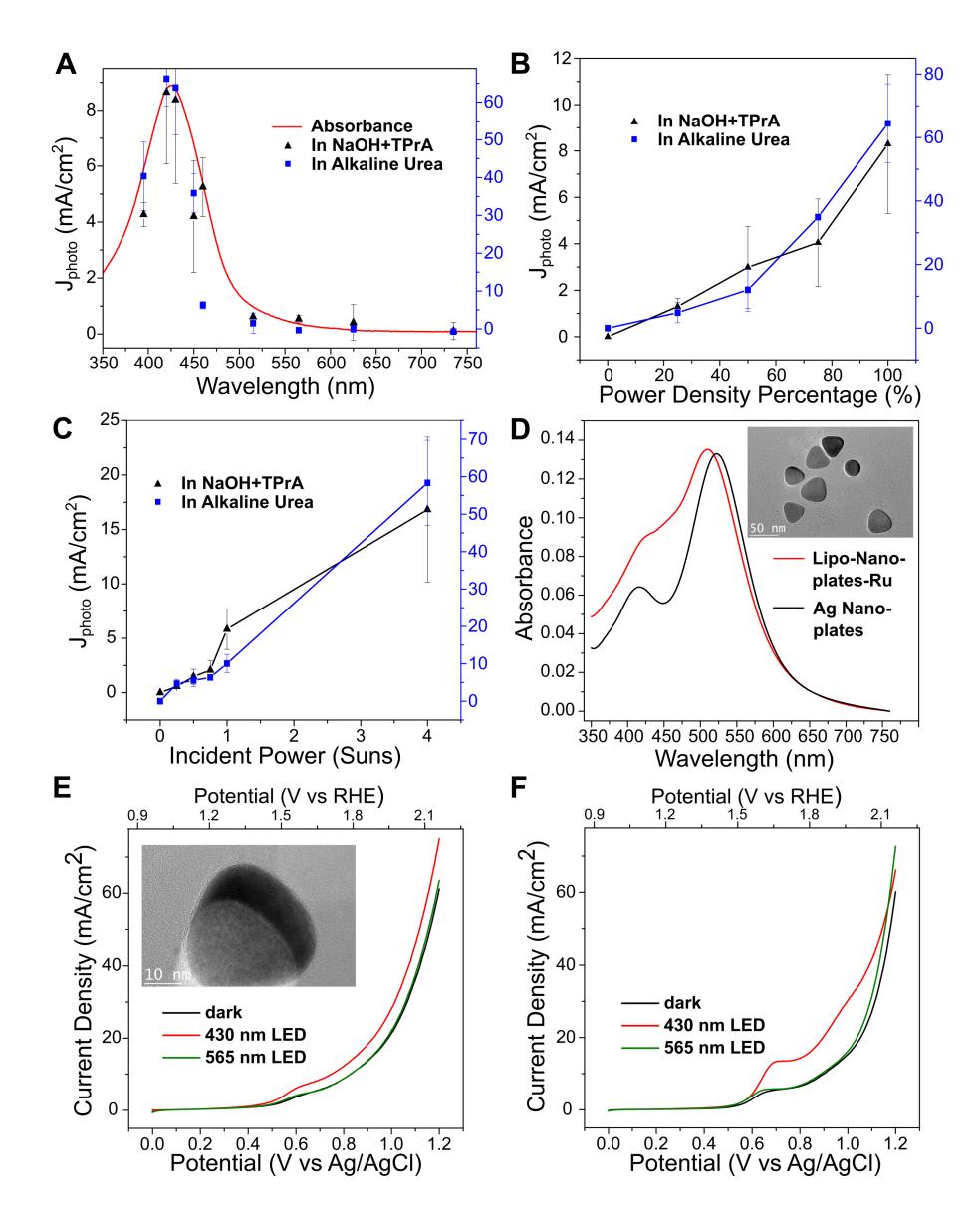


Figure 5. Electrochemical Characterization of Plasmonic Enhancement Mechanism.

(A) Plots of photocurrent density (J_{photo}) as function of wavelength of the incident light for nanopigments in NaOH+TPrA (black triangles) and alkaline urea (blue squares). J_{photo} is calculated from the LSV peaks at 650 mV in NaOH+TPrA and 750 mV in alkaline urea. The absorbance spectrum of the nanopigments (red) is added for comparison. Error bars are standard deviations of three measurements.

- (B) Plot of photocurrent densities as function of incident power density (430 nm LED) in NaOH+TPrA (black triangles) and alkaline urea (blue squares) electrolytes. 100% power density refers to the power used for all LSV measurements in **Figure 4** and **5A, E, F**. See also Supplemental Experimental Procedures. Error bars are standard deviations of three measurements.
- (C) Plot of photocurrent densities over different incident powers of a sunlight simulator in NaOH+TPrA (black triangles) and alkaline urea (blue squares) electrolytes. See also Fig. S4.
- (D) UV-vis absorbance spectra of Ag nanoplates (black) and membrane-wrapped Ag nanoplates with $[Ru(bpy)_3]^{2+}$ (Lipo-Ag Nanoplates-Ru) (red); Inset: TEM of Ag nanoplates; scale bar=50 nm.
- (E) LSV curves for Lipo-Ag Nanoplates-Ru in 0.1 M NaOH+0.01 M TPrA electrolyte without illumination (black), with 430 nm LED illumination (red) and with 565 nm LED illumination (green); Inset: TEM image of a Lipo-Ag Nanoplates-Ru particle with a visible lipid membrane; scale bar=10 nm.
- (F) LSV curves for Lipo-Ag Nanoplates-Ru controls in alkaline urea electrolyte in the dark (black), with 430 nm LED illumination (red) and with 565 nm LED illumination (green).

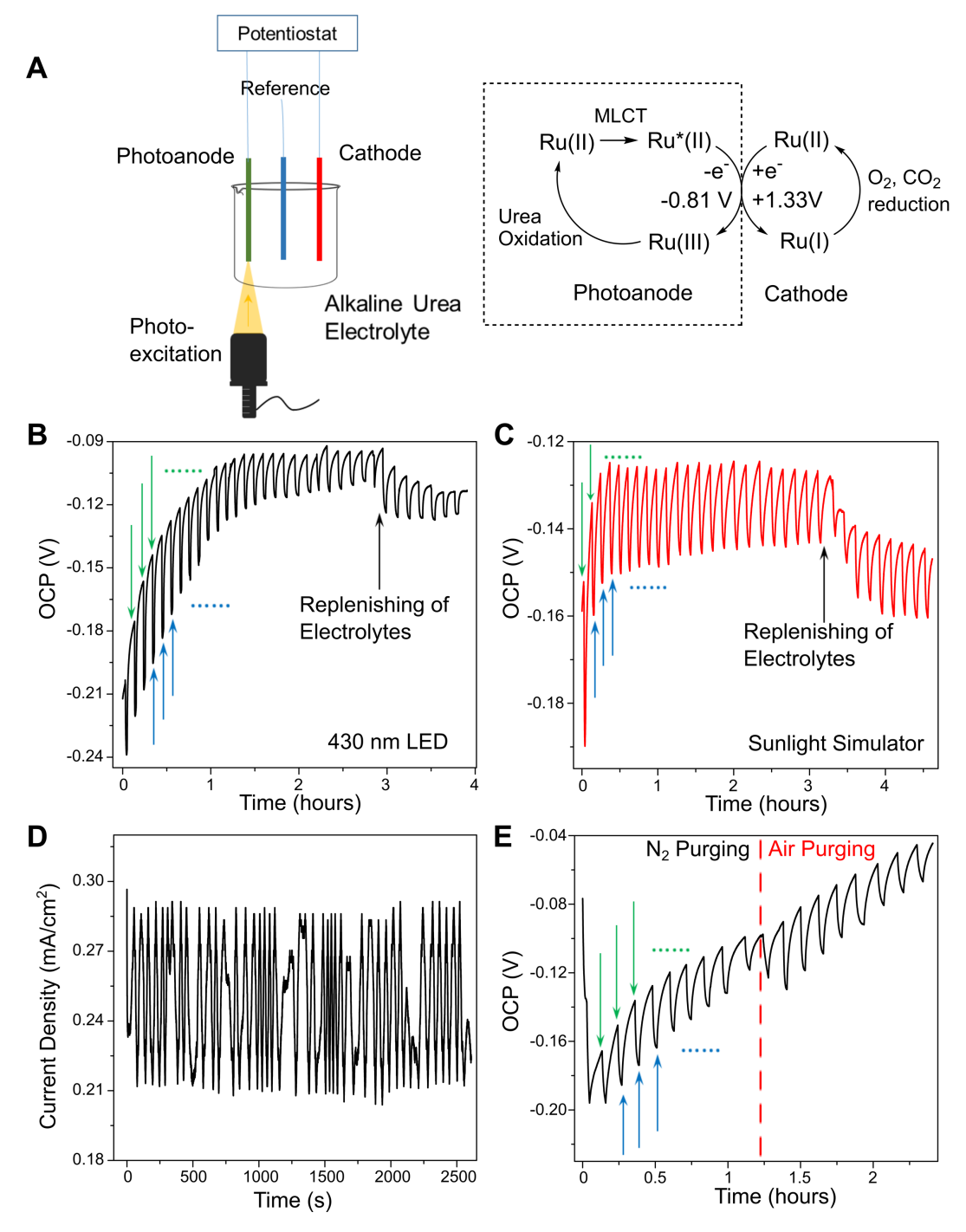


Figure 6. Characterizations of the Visible Light-Driven Direct Urea Fuel Cell (LDUFC).

(A) LDUFC whole cell setup and cell reactions scheme.

(B and C) Open Circuit Potential (OPC) measurements for nanopigments in 0.33 M Urea+0.1 M NaOH electrolyte with (B) 430 nm LED illumination or (C) sunlight simulator at 1-sun power illumination. Light On/Off cycles are indicated by green/blue arrows.

(D) Short Circuit Current density measurement under constant illumination with 430 nm LED.

(E) Open Circuit Potential (OPC) measurements for nanopigments in 0.33 M Urea+0.1 M NaOH electrolyte with 430 nm LED illumination and Nz/Air purging.





S1. Supplemental Data Items

S1.1 Assembly and Structural Characterization of Plasmonic Nanopigments

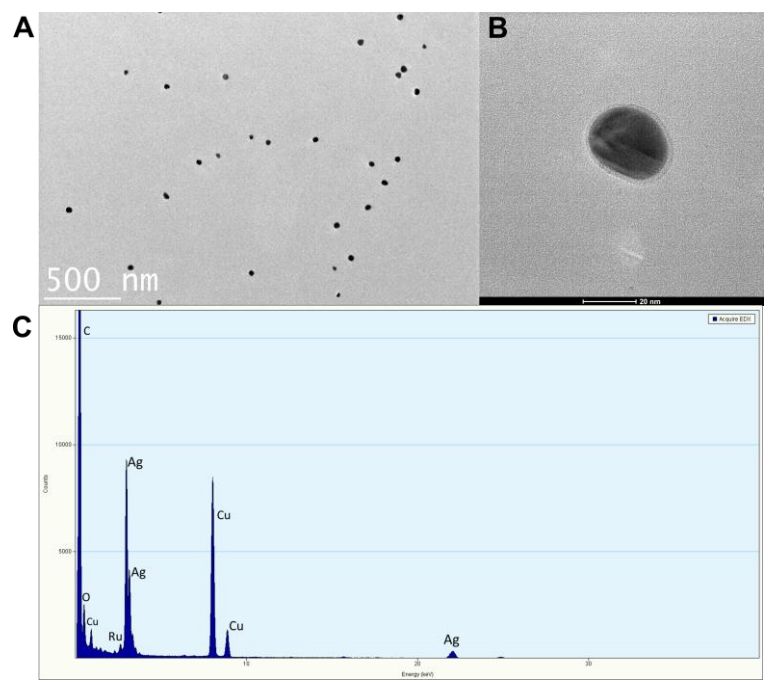


Figure S1. Structural Characterizations of the Nanopigments. Related to Figure 2B, C. D. E.

- (A) TEM image of an area with nanopigment particles. Scale bar=500 nm.
- (B) TEM image of a nanopigment particle with a clearly visible uniform membrane; scale bar=20 nm.
- (C) Energy Dispersive X-Ray Spectroscopy (EDX) spectra of the same imaging area in (B); C and O are from the lipid membrane and stabilizing ligands, Cu is from TEM grid used for imaging.

S1.2 Characterization of [Ru(bpy)₃]²⁺ Binding in the Lipid Membrane

Table S1. Characterizations of Nanopigments with Varying Input Percentages of [Ru(bpy)₃]^{2*}. The Percentage of 10 mol % (Red) Is Chosen for Nanopigments Characterizations in the Manuscript Unless Otherwise Noted.

Groups	Hydrodynamic Diameters (nm)	Zeta Potentials (mV)	Actual ¹⁰¹ Ru Concentrations (ppb)
"bare" Ag NPs	44.23±0.62	-28.2±1.7	N/A
LipoAg (o% Ru)	59.86±4.14	-41.9±3.0	N/A
2 mol % Ru	65.66±2.35	-40.7±2.2	128.33±2.60
5 mol % Ru	59.22±4.78	-37.0±2.0	213.33±3.18
10 mol % Ru	56.72±2.86	-30.9±1.4	382.15±29.90
13.3 mol % Ru	76.70±1.66	-27.2±4.8	527.89±9.90
16.7 mol % Ru	111.01±8.14	-20.0±0.5	819.94±27.57
20 mol % Ru	136.80±2.95	-13.7±0.2	856.79±96.87

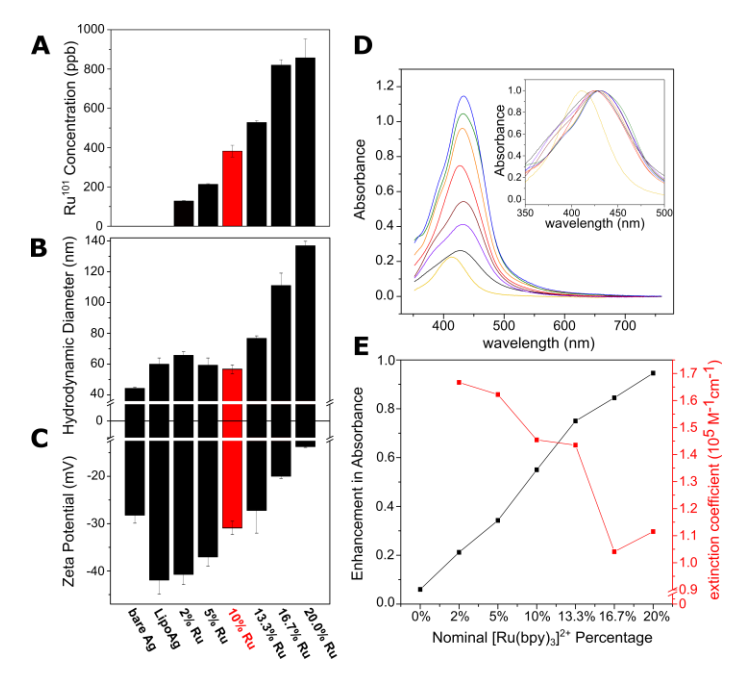


Figure S2. Characterizations of Nanopigments with Varying Input Percentages of $[Ru(bpy)_3]^{2^{+}}$.

(A) ICP-MS results of ¹⁰¹Ru concentrations for different [Ru(bpy)₃]²⁺ input percentages. ¹⁰¹Ru content increases steadily for input concentrations occurs up to 16.7 mol %. For even higher percentages, ¹⁰¹Ru concentrations shows weak additional increase, suggesting saturation of binding

(B) DLS results of hydrodynamic diameters for different $[Ru(bpy)_3]^{2+}$ input percentages. Nanopigments with 0-10 mol % $[Ru(bpy_3)]^{2+}$ increased moderately from that of the unwrapped "bare" Ag NPs due to lipid membrane wrapping. NP agglomeration is seen for nominal $[Ru(bpy_3)]^{2+}$ percentages > 13.3 mol %.

(C) Zeta potentials for different [Ru(bpy)₃]²⁺input percentages.

(D) UV-vis absorption spectra of Nanopigments with different $[Ru(bpy)_3]^{2+}$ input percentages. Color code: "bare" Ag NPs (yellow), LipoAg (black), 2% $[Ru(bpy)_3]^{2+}$ (violet), 5% (wine), 10% (red), 13.3% (orange), 16.7% (green), 20% (blue). An increasing trend in MLCT absorption band is seen with larger $[Ru(bpy)_3]^{2+}$ input percentages. Inset: Normalized spectra at MLCT absorption peak around 430 nm.

(E) Plot of Enhancement in absorbance at 430 nm (black) and calculated extinction coefficient (red) for Nanopigments with different [Ru(bpy)₃]²⁺input percentages.

Table S2. Characterizations of $[Ru(bpy)_3]^{2+}$ Binding in the Nanopigments. DLS Results of Nanopigment Hydrodynamic Diameters, Liposome Zeta Potentials before $[Ru(bpy)_3]^{2+}$ Binding, and ICP-MS Results of 101 Ru Concentrations. Related to Fig. 2F, G.

Groups	Hydrodynamic Diameters (nm)	Zeta Potentials (mV)	¹⁰¹ Ru Concentrations (ppb)
Nanopigments (5% DOPS)	56.72±2.86	-59.9±0.4	382.15±29.90
4% DOPS	57.89±1.34	-50.4±1.0	372.81±9.31
3% DOPS	64.35±5.73	-43.4±2.5	323.83±16.67
2% DOPS	69.40±1.59	-34.9±3.6	329.79±8.04
1% DOPS	102.13±11.56	-22.1±0.6	249.31±43.70
0% DOPS	342.67±1.36	0.2±0.1	347.16±16.04
5% EPC	80.10±4.52	8.5±2.6	172.96±26.58
10% EPC	63.36±2.85	43.2±2.1	179.09±0.16
PEG Passivated	63.79±10.97	-71.2±1.3	199.65±34.09

S1.3 Photophysical Characterizations of the Nanopigments and Controls

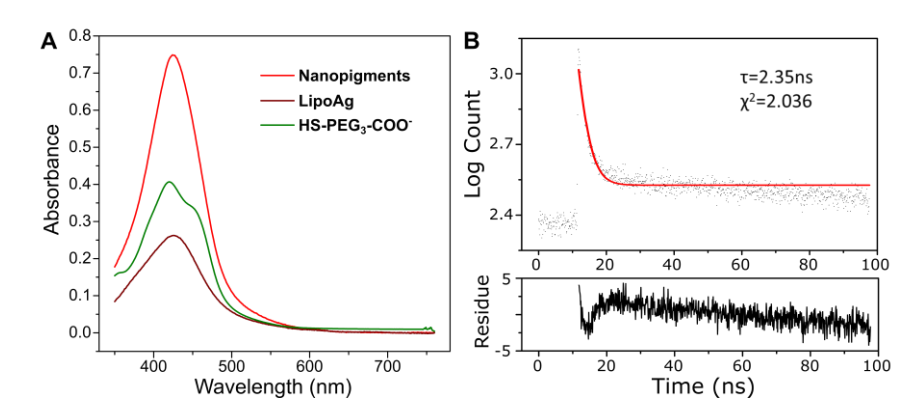


Figure S3. Photophysical Characterizations. Related to Fig. 3C, D.

(A) UV-vis absorbance spectra of water suspensions of the plasmonic nanopigments (red), LipoAg

(A) UV-vis absorbance spectra of water suspensions of the plasmonic nanopigments (red), LipoAg control without $[Ru(bpy)_3]^{2+}$ (brown) and the short HS-PEG₃-COO⁻ (Mw=238.3)-linked control with $[Ru(bpy)_3]^{2+} \sim 1$ nm from Ag surface. Enhancement in the PEG-linked group confirms incorporation of $[Ru(bpy)_3]^{2+}$.

(B) Photoluminescence decay pattern and emission tail fit curves (red) for the short HS-PEG₃-COO (Mw=238.3)-linked control.

S1.4 Validation of E-Field Enhanced Plasmonic Catalysis Mechanism

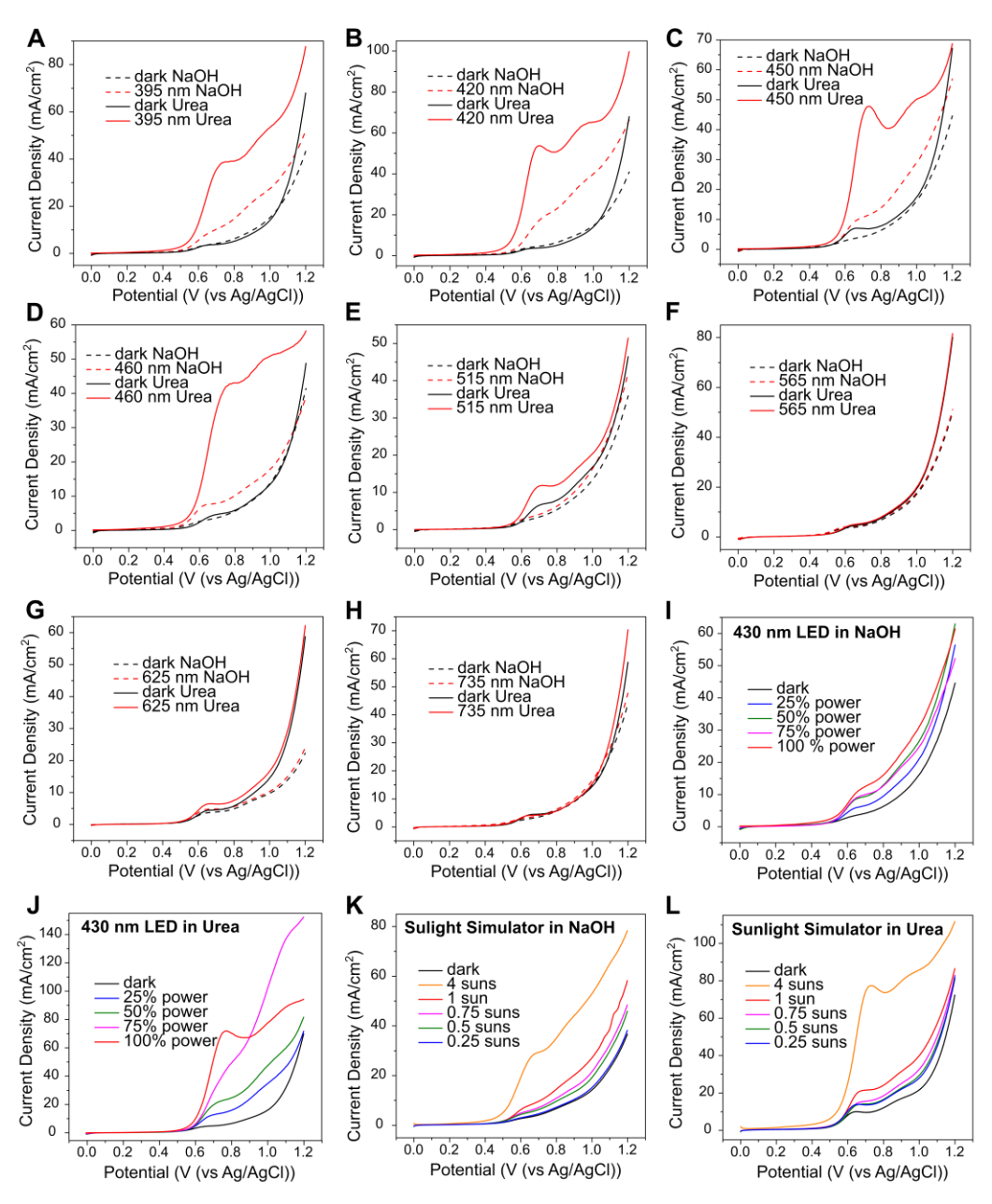


Figure S4. Electrochemical Characterizations for Plasmonic Enhancement Mechanism. Related to Fig. 5.

(A-H) LSV curves for wavelength-dependency studies in NaOH (0.1 M NaOH+0.01 M TPrA electrolyte) and Alkaline Urea (0.33 M Urea+0.1 M NaOH+ 0.01 M TPrA electrolyte). Focused LEDs with wavelengths 395 nm (A), 420 nm (B), 450 nm (C), 460 nm (D), 515 nm (E), 565 nm (F), 625 nm (G) and 735 nm (H) are used in respective panels.

(I, J) LSV curves for incident light power-dependency studies with a 430 nm LED in NaOH (I) and Alkaline Urea (J) electrolytes. 100% power refers to the max power density of the LED, 97. 65 W/m², as is used for LSVs in Fig. 4 and Fig. 5A, E, F.

(K, L) LSV curves for incident light power-dependency studies with a Sunlight Simulator in NaOH (I) and Urea (J) electrolytes.

S2. Supplemental Experimental Procedures

Preparation of the Plasmonic Nanopigments. A lipid thin film was first generated in round-bottom flasks through rotary evaporation of chloroform solutions of lipids mixed with a methanol solution of [Ru(bpy3)]Cl2 (Sigma Aldrich). Unless otherwise noted, input percentages were: 45 mol % of 1,2-dipalmitoyl-sn-glycero-3-phosphocholine (DPPC, Avanti Polar Lipids); 5 mol % of 1,2-dioleoyl-sn-glycero-3-phospho-L-serine (DOPS, Avanti Polar Lipids), 40 mol % Cholesterol (Avanti Polar Lipids) and 10 mol % of [Ru(bpy₃)]Cl₂ (Sigma Aldrich), with a total DPPC+DOPS+Cholesterol amount of 1 µmol. After overnight desiccation of the thin film in a flask, the lipids were re-dispersed with 1 ml of water and liposomes were generated through tip sonication under Argon purge. DLS tests on the liposome suspension after tip sonication show an average diameter of 117.3±5.2 nm. 80 µl 2mg/ml of octadecanethiol (Sigma Aldrich) in anhydrous ethanol is subsequently added into the liposome suspension in order to (1) increase the polarity of the dispersant to break apart the liposomes into lipid rafts for wrapping and (2) integrate the octadecanethiol molecules close to the tail groups of the lipids through hydrophobic interaction. 0.5 ml Aq NPs (Nanocomposix) colloid with approximately 1010 NPs and a hydrodynamic diameter of 44.23±0.62 nm (DLS) were subsequently mixed with liposomes/octadecanethiol suspension, where the thiol groups interact covalently with Ag surface and tether the lipid layers around the metal NPs. The 1.5 ml mixture was incubated on a shaker for 12 h before being washed twice by water and stored in 4 °C for later characterizations.

Assembly and Structural Characterizations of the Nanopigments. 16:0 Liss Rhod PE (1,2-dipalmitoyl-sn-glycero-3-phosphoethanolamine-N-(lissamine rhodamine B sulfonyl) (ammonium salt)) (Avanti Polar Lipids) with excitation/emission wavelengths at 560/583 nm was incorporated into the membrane of the nanopigments at 2 mol %. The input percentages of the other membrane components was adjusted to: 43 mol % DPPC, 5 mol % DOPS, 40 mol % cholesterol and 10 mol % [Ru(bpy)₃]²⁺. The following preparation procedures was identical to the above-mentioned process. Darkfield images and fluorescent images were taken on an Olympus IX71 Inverted Microscope and colocalization analyses were performed with Image J.

Dynamic Light Scattering (DLS) was measured on a Malvern Zetasizer in polystyrene cuvettes with 1 cm light path. Inductively-Coupled Plasma Mass Spectrometry (ICP-MS) measurements were taken by a VG Plasma Quad ExCell ICP-MS equipped with a Merchantek LUV213 Laser Ablation system. Colloidal nanopigments and control groups were diluted and dissolved by incubating in 1 ml aqua regia at 55°C. 5 ml 2% ICP-MS grade HCl was added to extract the dissolved elemental components. A calibration curve was constructed in each run with eight calibration samples respectively with Ag and Ru concentrations of 0.25 ppb, 0.5 ppb, 1 ppb, 2 ppb, 5 ppb, 10 ppb, 20 ppb, 50 ppb; the detected intensities were converted into concentrations using this calibration curve and the applied dilution factors. Transmission Electron Microscopy (TEM), high-resolution TEM (HRTEM), Scanning Transmission Electron Microscopy (STEM) images, Energy Dispersive X-ray (EDX) spectra and element maps were obtained on a Tecnai Osiris transmission electron microscope with a Super-X EDX detection system at an acceleration voltage of 200 kV. Statistical analysis on the membrane width was performed with Image J on 70 nanopigment particles from TEM images. 4 data points were obtained from each particle to account for fluctuations in membrane width on the same particle.

Characterization of [Ru(bpy)₃]²⁺ Binding in the Lipid Membrane. To study the effect of different surface charge, the amount of DOPS during nanopigment preparation was varied from 0 to 5 mol %; the amount of DPPC was varied accordingly to maintain a DPPC+DOPS nominal amount of 50 mol %. For nanocomposites with positively-charged surface, cationic lipid EPC (1,2-dioleoyl-sn-glycero-3-ethylphosphocholine, Avanti Polar Lipids) is added at 5 and 10 mol %, no DOPS is added, and a total EPC+DPPC amount is kept at 50 mol %. The rest of the preparation is identical to the nanopigments. To study the effect of hydrophobic interaction of the lipid layer, thiolated Polyethylene Glycol (PEG) with carboxyl end groups (HS-PEG-COOH, Mw=1000, Nanocs)-passivated Ag NPs with [Ru(bpy)₃]²⁺ was prepared: a 2 μmol water solution of thiol-PEG-COOH was mixed with a water solution of [Ru(bpy)₃]²⁺ and added to 10¹⁰ Ag NPs colloid to make a total volume of 1.5 ml. The mixture was incubated and mixed overnight. The resulting colloid was washed with water. To study the loading of [Ru(bpy₃)]²⁺, groups of nanocomposites with varying [Ru(bpy₃)]²⁺ input percentages from 0 to 20 mol % was made, where the total amount of DPPC+DOPS+Cholesterol was kept constant at 1 μmol. All groups were analyzed by DLS, ICP-MS and UV-vis spectrometry.

Photophysical Characterizations of the Nanopigment and Controls

UV-Vis Spectra was collected by a Cary 5000 Spectrometer in 350-760 nm range, with a scan rate of 10 nm/s. A 1 cm Quartz cell (Starna) was used in the measurement for all groups. Phosphorescence lifetime data were measured from an Edinburgh LifeSpec II lifetimer with a 405 nm excitation laser. Quantum Yield (QY) results were gathered by a Horiba Nanolog Spectrofluorometer with a 450 W Xenon lamp, a Synapse CCD camera and an integrating sphere setup. An excitation range of 420-440 nm and an emission range of 620-630 nm was used for integration and QY calculation.

The control group in photophysical characterization where $[Ru(bpy)_3]^{2+}$ is localized at around 1 nm from the Ag NPs is prepared in a similar approach as in the previous section. An estimated 10^{10} 44 nm Ag NPs added to a mixture water solution with 2 μ mol HS-PEG₃-COOH (Mw=238.3, Broad Pharm; Flory radius < 1 nm) and $[Ru(bpy)_3]^{2+}$. The mixture is incubated at room temperature for 12 hours before being centrifuged, washed with water and combined for characterizations.

Simulation Setup of [Ru(bpy)₃]²⁺ and Lipid Nanoparticle

The initial lipid monolayer structure was constructed with CHARMM-GUI¹ using the CHARMM36 force field²-³ containing 55 DPPC, 40 Cholesterol, and 5 DOPS molecules. The NP surface was modeled as a classical, flat FCC lattice with lattice constant of 4.08 Å for a total constant area of 97.92 Å². For computational efficiency, self-interactions within the lattice were turned off and the entire lattice was held rigid. OCT was bound to every other surface site on the lattice, for a total of 144 (12x12) molecules. A large amount of TIP3P water, with counter ions, was added to the system in order to prevent interaction of the membrane or [Ru(bpy₃)]²⁺ molecule with the above periodic image, totaling ~175 waters/lipid for an approximate height of 50 Å. Initially, the [Ru(bpy₃)]²⁺ molecule was placed into a cut-out in the water box, centered over the membrane surface. Ru-N bond parameters were approximated by existing CHARMM36 parameters for the Fe-N bond in Heme residues. All other parameters for [Ru(bpy₃)]²⁺ were obtained from the CHARMM generalized force field (CgenFF).⁴ The full system was assembled with Moltemplate.⁵ Molecular dynamics simulations were run using the LAMMPS software package 6 in the NPAT ensemble with T=298.0 K and Pz = 1 bar. A particle-particle particle-mesh (pppm) solver was used for Coulombic interactions⁷ and shake⁸ was used to constrain all bonds containing hydrogen. Equilibration was accomplished in several stages. First, the [Ru(bpy₃)]²⁺ was held fixed, above the membrane, while the water, lipids, and octadecanethiol were simulated for 60 ps. Second, the [Ru(bpy₃)]²⁺ complex was pulled into the membrane, approximately 1 nm from the NP surface, by applying a constant velocity to each particle (fix move) and ignoring the forces on [Ru(bpy₃)]²⁺ atoms (fix setforce). Finally, the Ru²⁺ center was held fixed in the membrane, still allowing for the ligands to fluctuate, and the entire structure was equilibrated for 5 ns.

Non-Equilibrium Simulation of [Ru(bpy)₃]²⁺ Binding in the Lipid Membrane

After initial equilibration, configurations with $[Ru(bpy_3)]^{2+}$ held in-membrane were taken every 0.5 ns for a total of 35 samples. Each configuration was given randomized velocities and the $[Ru(bpy_3)]^{2+}$ molecule was pulled along the z-axis with steered molecular dynamics using a $5x10^{-5}$ pull rate and a spring constant of 50.0 kcal/mol. The Jarzynski equality (**Eq. S1**) $^{9-10}$ relates the non-equilibrium work, W, calculated as the sum of the force pulled by the spring times its displacement for each simulation step, to the equilibrium free energy difference as

$$exp[-\Delta F/kT] = \overline{exp[-W/kT]}$$
 Eq. S1

where the overbar indicates an average, k is Boltzmann's constant, and T is the temperature.

Synthesis of Ag Nanoplates and Lipo-Ag Nanoplates-Ru Nanocomposite Control. Ag nanoplates were synthesized through a modified seed-mediated growth approach.¹¹ 20 ml 0.01 M AgNO₃ (Sigma Aldrich) in MilliQ water was mixed with 80 μl 0.1 M CTAB (cetrimonium bromide, Sigma Aldrich). Into this mixture, 0.6 ml 10mM NaBH₄ (Sigma Aldrich) was rapidly added all at once with fast stirring. Stirring was left on for 2 minutes before the solution was kept undisturbed in dark for 1 hour. This solution is then collected as the seed solution with 5 nm Ag NPs growth seeds. Growth solution is prepared by mixing 10 ml 10 mM CTAB, 0.25 ml 20 mM AgNO₃ and 0.5 ml 0.1 M ascorbic acid (Sigma Aldrich). Varying the amount of seed solution added into the growth solution could lead to different sizes of nanoplates. To get nanoplates

with widths around 40 nm, 0.25 ml of seed solution is added drop-wise into the growth solution with stirring. 0.1 ml 1 M NaOH is added subsequently with minor shaking to assist the growth. The final mixture is kept static for 1 hour for growth and separation of aggregated particles. The suspension is collected and washed twice with water through centrifugation. The product is a mixture of nanoplates with widths of 42.4±4.0 nm and nanospheres with diameters of 37.9±3.4 nm. The concentration of the nanoplates suspensions is estimated based on the absorption Optical Density and Beer-Lambert's law. 10¹⁰ nanoplates were accumulated into 0.5 ml and used for Lipo-Ag nanoplates-Ru composite synthesis in an identical approach as for the nanopigments. Both wrapped and unwrapped nanoplates are analyzed with DLS, UV-vis and TEM. Nanoplates have an average width of 42.4±4.0 nm.

Electrochemical Characterizations. Linear Sweep Voltammetry (LSV) curves and Chronoamperometry (CA) were measured with a potentiostat (Gamry Instruments) using a three-electrode system: a 3 mm-diameter Glassy Carbon (GC) working electrode, a standard Ag/AgCl reference electrode and a platinum wire counter electrode, all purchased from BASI Analytical Instruments. 10 μl water suspension of the nanopigments with ¹⁰⁷Ag (3937.35±153.33 ppb) and ¹⁰¹Ru (382.15±29.99 ppb) (from ICP-MS, **Table S1**) or control group NPs suspensions were drop casted onto the GC electrode and let dry for 2 hours in the dark. The Ag and Ru concentrations in all applicable groups are kept identical to the nanopigments. LSV curves were collected both in an alkaline electrolyte with 0.1M NaOH and 10 mM Tripropylamine (TPrA, Sigma Aldrich), and in an alkaline urea solution with 0.1 M NaOH + 10 mM TPrA + 0.33 M Urea. During the measurement, a collimated 430 nm LED (Thorlabs) with a power density of 97.65 W/m² was focused onto the GC working electrode. A scan rate of 50 mV/s and a collection rate of 10 Hz was used in LSV measurement; a potential of 650 mV (vs Ag/AgCl) and a collection rate of 1 Hz was adopted for the CA measurement. Conversion between Reversible Hydrogen Electrodes and Ag/AgCl scale is based on: E (vs RHE)=E (vs Ag/AgCl) + 0.059pH + E^o (vs Ag/AgCl), where the E^o (vs Ag/AgCl)=0.1976 and pH=13 is used.

Current density of the nanopigments and controls was calculated from the measured current and the total surface area (A) of nanopigments on the working electrode of 0.00381 cm². Surface area calculation was based on an average particle hydrodynamic diameter (d) of 56.72±2.86 nm (DLS) and a particle number calculated from Ag¹07 concentration of 3937.35 ppb (ICP-MS), average particle size, and a silver NPs density of 10.6 g/cm³ (Nanocomposix): the number of nanopigment particles in the 10 µl (V) suspension used on the electrode can first be calculated by dividing the total volume of NPs by the volume of each nanoparticle. The total volume can be calculated based on the following equation $V_{total} = \frac{c \times V \times 10^7}{10.6}$ and the volume of an individual nanoparticle can be calculated from d. A particle number of 3.77x107 is calculated. The total surface area can be calculated by multiplying the individual particle surface area with the particle number.

Tafel Plots are constructed based the Tafel Equation:

$$\eta = A \times ln \frac{i}{i_0},$$

where η is overpotential; A is the Tafel Slope; i is current density; and i_0 is exchange current density, the current at equilibrium and therefore the x-axis intercept in a Tafel Plot. A Tafel Plot is constructed based on the Linear Sweep Voltammetry curves and reflects the electrochemical kinetics relating the rate of reactions to potentials. It is a plot of the potentials around reaction onset against the log scale of current density. Therefore, Tafel Slope indicates the amount of potential input required for the reaction current density to have one magnitude of increase (unit increase on Log scale); and a smaller Tafel Slope is typically associated with more favorable intrinsic kinetics for the catalysis of the reactions of interest.

Calculations of Applied Bias Photo-to-Current Efficiency (ABPE). During electrochemical Linear Sweep Voltammetry, anode reaction is defined by Urea Oxidation (**Eq. S2**) while the cathode reaction is hydrogen evolution in alkaline conditions (**Eq. S3**), respectively with standard electrode potentials of E_1° and E_2° . The standard potential of the non-spontaneous urea oxidation electrolysis cell could be calculated by $E_{cell}^{\circ} = E_1^{\circ} + E_2^{\circ} = -1.29 \text{ V}$

Anode: $CO(NH_2)_2 + 6OH^- \rightarrow N_2 + 5H_2O + CO_2 + 6e^- E_1^0 = -0.46 V$

Incident LED power was measured to be 105 mW using a Thorlabs PM100A powermeter with the same electrode setup; after correcting the focused beam area (18.5 mm in diameter) for the area of the glassy carbon (3.0 mm in diameter) on the GC electrode, an effective light power P_{eff} was measured to be 2.76 mW, with a power density of 97.65 W/m². A maximum Applied Bias Photon-to-current Efficiency (ABPE) could be observed at $|V_{bias}|$ =750 mV, where there is a maximum photocurrent I_{pho} =0.21 mA. A maximum Applied Bias Photo-to-current Efficiency (ABPE) could be calculated to be 4.1% from **Eq. S4** based on photocurrent I_{pho} , P_{eff} and V_{bias} .

$$ABPE = \frac{I_{pho} \times (|-1.29 V| - |V_{bias}|)}{P_{eff}} \times 100\%$$
 Eq. S4

Illustration of E-Field-Enhanced Plasmonic Catalysis Mechanism. Wavelength-dependency of plasmonic catalysis studies were carried out by LSV measurements in three-electrode setups as previously described with different incident wavelength or light power. 0.1 M NaOH+0.01 M TPrA and 0.33 M Urea+0.1 M NaOH+ 0.01 M TPrA electrolytes were both studied. Focused LEDs with wavelengths of 395 nm, 420 nm, 430 nm, 450 nm, 460 nm, 515 nm, 565 nm, 625 nm, 735 nm (ThorLabs) were used respectively as light sources. The photocurrent densities at 650 mV (vs Ag/AgCl) were calculated for NaOH+TPrA electrolyte, while those at 750 mV (vs Ag/AgCl) were calculated for alkaline urea electrolyte. Intensity-dependency measurements were carried out with a 430 nm LED and a sunlight simulator (Newport Oriel High Power Digital Solar Simulator, Newport Model 67005 Arc Lamp). For the 430 nm LED, a max power density of 97.65 W/m², which is used for LSV measurements in Fig. 4 and Fig. 5A, E, F is set as 100%, and LSVs gathered in dark is set as with 0% incident power. 25%, 50% and 75% power is used in between. For the sunlight simulator, 1-sun power is defined as the nominal full sunlight intensity on a bright clear day on Earth, equaling to 100 mW/cm². Powers equivalent to 0.25 suns, 0.5 suns, 0.75 suns, 1 sun and 4 suns were used. Three repeats were recorded to calculate the standard deviation. Linear Sweep Voltammetry of the Lipo-Ag nanoplates-Ru was carried out in dark, with 430 nm and with 565 nm LED

Calculation of Photothermal Temperature Increase of Nanopigments. The temperature increase of a spherical metal NP upon illumination can be calculated based the following equation **Eq. S5** ¹²:

$$\Delta T = \frac{Q}{4\pi K_s R}$$
 Eq. S5

where K_s is the thermal conductivity of surrounding medium; R is the Radius of the metal sphere; Q is absorbed heat power and can be calculated by a multiply of the NPs absorption cross section (σ_{abs}) and irradiance light power density (I) (**Eq. S6**):

$$Q=\sigma_{abs}I$$
 Eq. S6

To calculate the absorption cross section of Ag NPs, the total extinction cross section (σ_{ext}) of Ag NPs can first be calculated based on the following equation:

$$\sigma_{\text{ext}}(\lambda) = B(\lambda)d^3 + D(\lambda)d^6$$
 Eq. S7

where B and D are parameters relating to the permittivity of the NPs and wavelengths of incident illumination. For Ag NPs with diameters less than 80 nm, B=(1.5±0.2)x10⁸x λ^{-1} and a D=0.¹³ At λ =430 nm illumination and a hydrodynamic NPs diameter d=44.23 nm, σ_{ext} (430 nm)=3.02x10⁻⁸ m² could be calculated. The absorption cross section σ_{abs} is related to σ_{ext} by

$$\sigma_{abs}$$
= $\Psi\sigma_{ext}$ Eq. S8

where Ψ is fractional thermal load. Ψ has been reported for Ag NPs with d<50 nm to be 0.126. Therefore, σ_{abs} could be calculated to be 3.78x10-9 m².

The 430 nm LED we used generated incident light power of 105 mW over a 18.5 mm diameter light spot; a incident power density (I) could be calculated accordingly to be 97.65 W/m². The thermal conductivity of lipid bilayers in water suspensions (K_s) have been reported to be close to 0.46 Wm⁻¹K⁻¹. And the Radius of the NPs R=22.12 nm. After applying σ_{abs} and I into **Eq. S6**, we calculate a Q=3.69x10⁻⁷ W. Apply Q, R, K_s into **Eq. S5**, a ΔT =2.89 K could be calculated.

Implementation and Characterization of the Visible Light-Driven Direct Urea Fuel Cell (LDUFC). A Visible Light-Driven Direct Urea Fuel Cell was constructed using GC electrodes with the nanopigments as both photoanode and cathode. The preparation of GC electrodes with nanopigments was with the same procedure as in Electrochemical Characterizations. The initial electrolyte was an alkaline urea solution with 0.1 M NaOH + 0.33 M Urea. No sacrificial reagents was needed since the cell reaction itself spontaneously replenished the steady state Ru(II) catalysts. A 430 nm LED or a sunlight simulator at 1-sun illumination (100 mW/cm²) was focused onto the working electrode as a photoanode while the counter electrode (cathode) was not illuminated. Open Circuit Potential (OCP) and photocurrent were measured by a Princeton Applied Research VersaStat 4 potentiostat. Control group with nitrogen purging were measured after 20 min pre-measurement purging and with purging during measurement in the same cell setup. For OCP measurement 150s/350s LED on/off cycles were adopted after an initial 300s stabilization time, and the Cell Voltage and OCP were recorded by the potentiostat. For photocurrent measurement, chronoamperometry mode was used with a 0V potential input to record the short circuit current (Isc) with constant illumination as function of time.

The IPCE for the visible light primary cell could be calculated from **Eq. S9** based on the effective power of illumination (P_{eff} =2.76 mW) and the short circuit current. With an average photocurrent density (J_{sc}) of 0.25 mA/cm² and a surface area of 0.00381 cm² (A) as calculated above, the IPCE% of the cell was calculated to be 0.1%.

$$IPCE = \frac{I_{sc}}{P_{eff}} \times \frac{1240}{\lambda(nm)} \times 100 = \frac{J_{sc} \times A}{P_{eff}} \times \frac{1240}{\lambda(nm)} \times 100$$
 Eq. S9

Supplemental References

- 1. Jo, S.; Kim, T.; Iyer, V. G.; Im, W., CHARMM GUI: a web based graphical user interface for CHARMM. *Journal of computational chemistry* **2008**, *29* (11), 1859-1865.
- 2. Vanommeslaeghe, K.; Hatcher, E.; Acharya, C.; Kundu, S.; Zhong, S.; Shim, J.; Darian, E.; Guvench, O.; Lopes, P.; Vorobyov, I., CHARMM general force field: A force field for drug like molecules compatible with the CHARMM all atom additive biological force fields. *Journal of computational chemistry* **2010**, *31* (4), 671-690.
- 3. Klauda, J. B.; Venable, R. M.; Freites, J. A.; O'Connor, J. W.; Tobias, D. J.; Mondragon-Ramirez, C.; Vorobyov, I.; MacKerell Jr, A. D.; Pastor, R. W., Update of the CHARMM all-atom additive force field for lipids: validation on six lipid types. *The journal of physical chemistry B* **2010**, *114* (23), 7830-7843.
- 4. Huang, J.; MacKerell Jr, A. D., CHARMM36 all atom additive protein force field: Validation based on comparison to NMR data. *Journal of computational chemistry* **2013**, *34* (25), 2135-2145.
- 5. Jewett, A. I.; Zhuang, Z.; Shea, J.-E., Moltemplate a coarse-grained model assembly tool. *Biophysical Journal* **2013**, *104* (2), 169a.
- 6. Plimpton, S., Fast parallel algorithms for short-range molecular dynamics. *Journal of computational physics* **1995**, *117* (1), 1-19.
- 7. Hockney, R. W.; Eastwood, J. W., Computer simulation using particles. crc Press: 1988.
- 8. Ryckaert, J.-P.; Ciccotti, G.; Berendsen, H. J., Numerical integration of the cartesian equations of motion of a system with constraints: molecular dynamics of n-alkanes. *Journal of computational physics* **1977,** *23* (3), 327-341.

- 9. Jarzynski, C., Nonequilibrium equality for free energy differences. *Physical Review Letters* **1997**, *78* (14), 2690.
- 10. Jarzynski, C., Equilibrium free-energy differences from nonequilibrium measurements: A master-equation approach. *Physical Review E* **1997**, *56* (5), 5018.
- 11. Jana, N. R.; Gearheart, L.; Murphy, C. J., Wet chemical synthesis of silver nanorods and nanowires of controllable aspect ratioElectronic supplementary information (ESI) available: UV–VIS spectra of silver nanorods. See http://www.rsc.org/suppdata/cc/b1/b100521i. Chemical Communications 2001, (7), 617-618.
- 12. Baffou, G.; Quidant, R., Thermo plasmonics: using metallic nanostructures as nano sources of heat. *Laser & Photonics Reviews* **2013**, *7* (2), 171-187.
- 13. Hlaing, M.; Gebear-Eigzabher, B.; Roa, A.; Marcano, A.; Radu, D.; Lai, C.-Y., Absorption and scattering cross-section extinction values of silver nanoparticles. *Optical Materials* **2016**, *58*, 439-444.
- 14. Yguerabide, J.; Yguerabide, E. E., Light-scattering submicroscopic particles as highly fluorescent analogs and their use as tracer labels in clinical and biological applications: II. Experimental characterization. *Analytical biochemistry* **1998**, *262* (2), 157-176.
- 15. Nakano, T.; Kikugawa, G.; Ohara, T., A molecular dynamics study on heat conduction characteristics in DPPC lipid bilayer. *The Journal of chemical physics* **2010**, *133* (15), 154705.